CrystEngComm

Accepted Manuscript

ROYAL SOCIETY OF CHEMISTRY

www.rsc.org/crystengcomm

Oxide based nanostructures for photocatalytic and electrocatalytic applications

Aparna Ganguly[a], Oruganti Anjaneyulu [b], Kasinath Ojha[b] and Ashok K Ganguli[a,b,c] *

[a]Nanoscale Research facility, Indian Institute of Technology Delhi, Hauz Khas, New Delhi-110016, India.

[b]Department of Chemistry, Indian Institute of Technology Delhi, Hauz Khas, New Delhi-110016, India.

[c]Institute of Nano Science & Technology, Habitat Centre, Phase- X, Sector – 64, Mohali, Punjab–160062, India.

*Corresponding author: email: ashok@chemistry.iitd.ac.in ; ashok@inst.ac.in phone- +91-11-2659-1511, fax: +91-172-2211074.

Abstract

Diminishing fossil fuels and global warming issues have forced the scientists to look for alternate sources of energy to cater to the ever increasing demand. Artificial systems are being developed in order to mimic natural photosynthesis and directly harvest and convert solar energy into renewable energy and environmental remediation. Despite significant efforts, it has been not possible to design a single material which has sufficient efficiency, stability and low cost. To integrate the desired characteristics in a single component, heterogeneous photocatalysts are designed with multiple functional components which could combine the advantages of different components to overcome the drawbacks of single component photocatalysts. The present highlight gives a concise overview of heterogeneous catalysts that have been developed and studied in our group and some excellent works of others in recent years. The review focuses on the principles of photocatalytic and electrocatalytic activity followed by the some key examples of oxide based materials. This includes a wide range of structural modification and crystal growth leading to composites, heterostructures, including insulator/semiconductor, semiconductor/semiconductor, and multi-hetero nanostructures and core-shell nanostructures which have been modified in order to improve the performance by increasing the light absorption, promoting the charge separation and transportation, enhancing the redox catalytic activity and intrinsic electrocatalytic properties. The electrochemical processes like hydrogen

evolution reaction (HER), oxygen evolution reaction (OER) and oxygen reduction reaction (ORR) have been discussed closely on the effect of size, shape, exposed facets and surface area of electrocatalysts (metal oxides).

Energy, environment & catalysis: An Introduction

The incessant rise of world's population together with extensive industrial development has led to energy crisis and environmental contamination. This rapid change resulted in depletion of natural sources like fossil fuels and the associated environmental problems like hazardous wastes, contaminated ground water and toxic air contaminants. The major challenge of 21st century material chemists is to find solution for all these problems[1a]. In order to address this significant problem, extensive research is underway to develop advanced analytical, biochemical, and physicochemical methods for the characterization and elimination of hazardous chemical compounds from air, soil, and water. Catalysis is one of the best approaches towards a solution for energy conversion (or) transformation of hazardous chemical wastes. In 1835, Jöns Jakob Berzelius coined the term "Catalysis". Ostwald was awarded Nobel Prize for his investigations on reactions catalyzed by presence of acids and bases in 1909. It may be noted that the Haber's process for ammonia synthesis (using heterogeneous catalysis) has been hailed as the most significant research of the 21st century[2]. Since heterogeneous catalysis is essentially a surface phenomenon, any property which affects the surface of the materials affects the catalytic property.

Nanotechnology is governed by miniaturization of materials with an aim to achieve improved properties compared to their bulk materials especially increasing the surface area for catalytic applications[3-8]. Change in particle size tends to influence the structural characteristics[9] and electronic properties of materials which in turn drives the physical and chemical properties of the material[10, 11]. Especially, the size and morphology dependent properties of nanomaterials, like the quantum confinement effects in semiconductor nanostructures and plasmonic absorption characteristics in metallic nanostructures, gains attention owing to its potential in developing new solar energy harvesting processes[12, 13].

Diverse nanostructures such as nanoparticles, porous nanospheres, nanotubes, nanorods, nanowires and other more complex structures have shown extraordinary unconventional properties, which enriches the material selection and can be chosen for the design of effective

photocatalytic systems. Nanoscale photocatalysts, with a large surface area, can contribute more active sites for desired reactions.

Herein this review, we briefly discuss the underlying principles of photo & electrocatalysis, the challenges faced while designing a catalyst with a focus on some of the recent studies done by our group as well as by other eminent groups on oxide based heterostructures including semiconductor/semiconductor, metal/semiconductor and also by varying the morphology of the nanomaterials. With the broad range of nanostructures available, the integration of multiple functional components has been easier to create heterogeneous structures with unique characteristics and enhanced performance. Conversion of solar energy into fuels and/or electricity is one of the major scientific challenges being faced by the researchers and is the need of the hour[14].

1. Photocatalysis

Photo catalysis involves the formation of energy rich electron-hole pairs from a semiconductor on the absorption of photons typically in UV-Visible range. The catalytic material should be photostable, inexpensive, non-toxic and also chemically and biologically inert[15].

The three major potential applications addressed by the phenomenon of photocatalysis are solar water splitting, photoreduction of CO_2 and photocatalytic detoxification of organic pollutants.

Also, there are three basic steps which follows after a semiconductor photocatalyst is exposed to incident photons either equal or larger than the band gap (Eg) of the semiconductor, a) photoexcitation of charge carriers i.e. excitation of an electron from the valence band (VB) of the semiconductor to its conduction band (CB) b) separation and diffusion of the charge carrier to the photocatalyst surface; and 3) oxidation and reduction reaction on the catalyst surface. The fate of the photoexcited electron on the photocatalyst surface can be different, for example, it might be used to reduce protons to hydrogen or oxygen to O^{2-} radicals, or even be used for reducing CO_2. Figure 1 depicts the possible processes on irradiating the metal oxide nanoparticle.

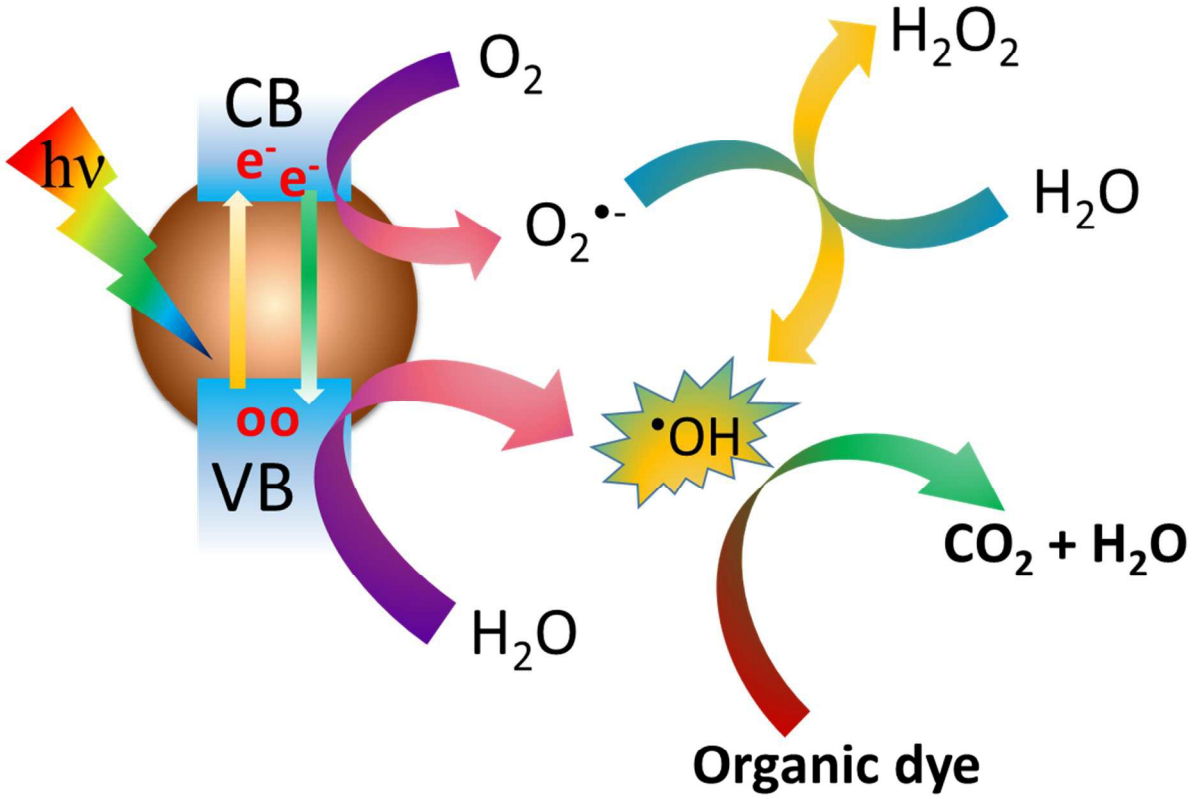

Figure 1. Schematic diagram of radical generation and organic dye degradation upon photoirradiation of a metal oxide semiconductor in water containing an organic dye.

However, for all these reactions to happen, the position of the CB & VB is critical. It is imperative that the CB minimum is located at more negative potential than the electrochemical potential of the desired reaction while the top of the valence band must be more positive than the oxidation potential of H_2O to O_2 (1.23 V vs. NHE). Thus, the minimum photon energy which is required to drive the reaction, thermodynamically calculated is 1.23 eV, and corresponds to a wavelength of ca. 1000 nm, in the near infrared region.

This value of 1.23 V per electron arises from the corresponding equations of oxidation and reduction of water (Eqs. (2) and (3), respectively).

$H_2O \rightarrow H_2 + ½\ O_2$ 1.23 V ----------(1)

$2H_2O \rightarrow O_2 + 4H+ + 4e^-$ 0.80 V/pH = 7 ----------(2)

$2H_2O + 2e- \rightarrow H_2 + 2OH^-$ −0.42/pH = 7 ----------(3)

This is a typical "uphill reaction" and involves a large positive change in the Gibbs free energy $\Delta G^{\circ} = 238$ kJ mol^{-1} which is essentially provided by light or ideally sunlight to drive the reaction [16, 17].

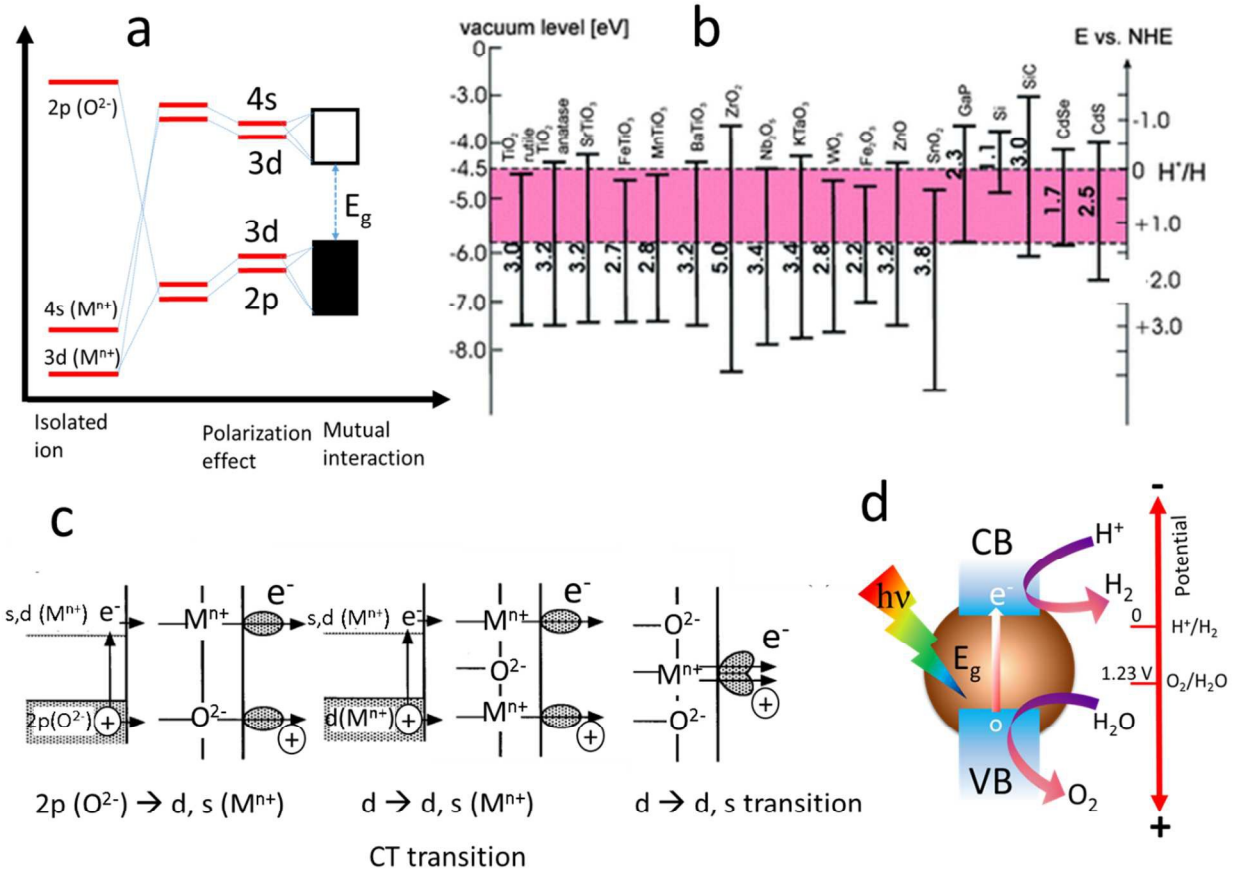

Figure 2. (a) Model of the band formation of an oxide semiconductor. (b) The band gaps and band-edge positions of several semiconducting photocatalysts relative to the vacuum level and the redox potentials for water photolysis Reproduced from Ref. 18 with permission from The Royal Society of Chemistry. (c) Charge transfer site at the surface of an oxide semiconductor (Figure a and c have been reproduced from Ref. 19 with permission from Elsevier). (d) Schematic of photocatalytic water splitting in presence of semiconductor.

The fundamentals of photocatalysis, especially its thermodynamics and kinetics of the process are essentially important to understand for the designing of an effective photocatalyst. In an excellent review by Prof. Ohtani, the important issues like the band position, activation energy, and rate determining step involved are discussed[20]. Apart from this, there exists a strong probability of recombination during the separation and diffusion process. The major pathway being the relaxation of photoexcited electrons back into the VB. Electrons also get trapped both

at and below the surface of a semiconductor, from where the recombination can proceed. Defects in the crystal structure or grain boundaries are usually the places where the holes can get trapped. The recombination probability can be minimized by improving the crystallinity of photocatalyst, as the density of crystal defects (trapping & recombination sites) is reduced with increasing crystallinity. The reduction in the particle size of the photocatalyst is also helpful since the diffusion pathway between the photoinduced charges and the reaction site is shortened.

Although, the last decade has seen some significant progress made in the area of photocatalysis, there are major issues that need to be addressed before photocatalysis can be both efficiently and economically used for commercial applications. The designing of photocatalyst essentially needs to consider the i) electronic structure ii) surface structure and iii) crystal structure which directly affects its performance. Other than photostability, there are two major concerns which should be taken into consideration for the development of a photocatalyst: first being the general improvement of light absorption (increase in photons absorbed), and the second being the extension of wavelength range for light absorption of semiconductor materials into the visible portion of the solar spectrum.

Some of the excellent reviews discuss the energetics of the photochemical & photoelectrochemical splitting of water using semiconductors[16]. Among all the classes of materials, metal oxides play significant role in several branches of chemistry, physics, biology and materials science. Metal oxides are one of the most enthralling classes of inorganic solids with diverse structures, properties and several applications in microelectronics, sensors, piezoelectric devices, phosphors, coatings, fuel cells, energy storage/conversion devices, coatings and extensively as catalysts[21-23]. Thus, the focus of this review remains mainly on metal oxides in form of heterostructures with other semiconductors.

Among the very first materials which has been studied for photocatalysis, is TiO_2. In the Honda–Fujishima effect[24] water oxidation was carried out on n-type TiO_2 single-crystal electrode by band-gap excitation in the early 1970s, and since then many researchers have explored the utility of TiO_2 as a photocatalyst due to its photoactivity, higher stability environment friendly and lower cost[25].

1.1 Metal Oxide photocatalysts

The two main groups of elements that can act as active cation components in a water-splitting metal oxide photocatalyst are group 4/5/6 and 13/14/15 elements i.e. Ti, V, Zr, Nb, In, Sn, Sb. TiO_2 and ZnO are both characterized by suitable band gap energy and favorable band positions which triggered the enormous amount of research on these two materials and still continues in the form of their composites. Among other materials, TiO_2 was among the first to be explored in detail. It crystallizes in three structure types: Rutile, Anatase, and Brookite. All modifications contain TiO_6 octahedra that are interconnected via two (Rutile), three (Brookite), or four (Anatase) common edges and via shared corners, and as a result, the band gaps (3.0 eV for Rutile and 3.15 eV for Anatase) differ slightly[26]. They also differ in their photo activity i.e. in general, nanostructured anatase displays better photocatalytic activity than those of Rutile[27]. In an effort to study the effect of a specific plane on photoactivity , Bahnemaan et al have carefully chosen a natural mineral from which a single crystal has been cleaved, polished and oriented for (101) surfaces for anatase whereas (001), (100), and (110) surfaces were chosen for rutile. The photocatalytic activities of the different TiO_2 single crystal surfaces have been assessed. A higher activity is observed towards the photocatalytic methanol oxidation on the anatase (101) surface as compared with that on the rutile (001) surface which can be explained either by direct interfacial transfer of photogenerated holes leading to the photocatalytic oxidation of methanol or the photogenerated OH• radicals on the anatase (101) surface are more reactive than those on the rutile (001) surface[27]. Batzill discusses the variation of photocatalytic activity of metal oxides as a function of their crystallographic surface orientation[17].

However, a serious limitation that remains with TiO_2 based photocatalysts is its large band gap ($E_g > 3$ eV) which can only absorb photons with light wavelengths shorter than about 400 nm in the UV or near-UV wavelength regime, which accounts for less than 5% of the total solar energy irradiation. Despite significant efforts, most photocatalysts available to date can only function in the ultraviolet (UV) or near UV regime with limited efficiency due to a number of limiting factors such as a mismatch between the semiconductor band gap and the solar spectrum, inefficient charge separation and transport, and the uncontrolled semiconductor degrading side reactions which lead to material instability[28]. Different methods have been explored to enhance light absorption in the visible light region, which include: (1) chemical doping of TiO_2, such as incorporation of additional metal or nonmetal species (e.g., nickel, vanadium, chromium, platinum, nitrogen, tungsten, fluorine, sulfur, etc.)[24, 29, 30] (2) the exploration of alternative

narrow band gap semiconductor photocatalysts, such as Si,[31] InP,[32] CdSe,[33] and GaZnON[34, 35] and (3) the loading of the visible light sensitizer, such as organic dye, metal nanoparticles, or a narrow band gap semiconductor.

Among the three phases (Rutile, Anatase and Brookite) of TiO_2, Anatase is the most widely studied[36, 37]. To improve the activity of TiO_2, p-block elements were substituted at Ti or O sites[38-41] or noble metals like Au or Pt were deposited on TiO_2 surface[42-45]. Wang et al studied the incorporation of TiO_2 with graphene or graphene oxide to enhance the adsorption ability and photodegradation of organic dyes[46]. The report of ZnO photocatalysis by Morrison and Freund used current doubling for the detection of hole and free-radical based reactions and capacity method for the detection of electron based reactions[47]. Rao and coworkers recently reported the photocatalytic hydrogen generation by the ZnO hybrid with cadmium chalcogenides along with Pt metal[48]. Considerable amount of hydrogen has been generated photocatalytically using the hybrid nanostructures of ZnO/Pt/CdS, ZnO/Pt/$Cd_{1-x}Zn_xS$ and ZnO/Pt/$CdS_{1-x}Se_x$, under UV-visible and visible light irradiation in the presence of hole scavengers like Na_2S and Na_2SO_3. The presence of a metallic contact between two semiconductors favors exciton charge separation. Good H_2 evolution rates up to 17.4 mmol $h^{-1}g^{-1}$ and an apparent quantum yield (AQY) of 11.1% were obtained with ZnO/Pt/CdS under UV-visible irradiation. With 20% Zn substitution in place of Cd in CdS, the rate of H_2 generation was 31.2 mmol h^{-1} g^{-1} and 12.5 mmol h^{-1} g^{-1} respectively with UV-visible and visible irradiation, the corresponding AQY values being 23.1% and 18%. While with 50% substitution of S by Se in CdS, the rate of hydrogen generation was at 19 mmol $h^{-1}g^{-1}$ and 16 mmol h^{-1} g^{-1} with UV-visible and visible irradiation respectively, but the AQY values were in the range of 8–9%. The catalytic activity was found to improve on replacing Na_2S and Na_2SO_3 by benzyl alcohol as the scavenger for ZnO/Pt/CdS yielding H_2 at the rate of 31.6 mmol h^{-1} g^{-1} and AQY of 34.5% under visible irradiation. The performance was even better with ZnO/Pt/$Cd_{0.8}Zn_{0.2}S$ where the rate was 36.5 mmol $h^{-1}g^{-1}$ and the AQY reached 50.4% with visible irradiation[48].

Hydrogenated ZnO (denoted H:ZnO) NRAs(Nanorod Arrays) were grown on a solid substrate and were used as photocatalysts for hydrogen evolution[49]. The advantage with high aspect ratio nanorods is that a large surface area is accessible for charge transfer and a short diffusion length for minority carriers and a long pathway for light absorption along the NR axis[50, 51]. On immobilizing the NRs on a substrate it prevents its aggregation and eases the separation and

recovery processes for ZnO powder catalysts. Surface defects such as oxygen vacancies (V_O) and interstitial hydrogen (H_i) were introduced purposefully into ZnO via hydrogenation process. These impurities assist in increasing the carrier density of ZnO which facilitate the transport of photoexcited charge carriers. Vertically aligned nanorods of H:ZnO with an average diameter of ~ 200 nm and length of ~ 2 mm were grown on an FTO glass substrate by cathodic electrodeposition followed by hydrogenation and annealing in air at 350°C .

The rate of hydrogen production was examined for H: ZnO NRAs in a Na_2S–Na_2SO_3 electrolyte solution under white light illumination (a 300 W xenon lamp without filter). While the ZnO sample has average hydrogen production rate of ~ 10 mmol h^{-1} cm^{-2}, the H: ZnO sample shows a 5-fold increase in hydrogen evolution, achieving a remarkable production rate of 49 mmol h^{-1} cm^{-2}. This has so far been reported to be the best photocatalytic hydrogen evolution rate ever for ZnO catalysts[52-55] which is about 40 times larger than the other values[52]. The photocatalytic activity of the hydrogenated NR powders were also determined in order to directly compare the reported values for ZnO powder. 1.64 mg of H: ZnO NR powders, equivalent to the mass loading on two pieces of H: ZnO NRA films, were collected from FTO substrates. The photocatalytic properties of these powders were measured under the same conditions as for H:ZnO NRA films. The hydrogen production rate of H: ZnO NR powders were calculated to be 18.8 mmol h^{-1} cm^{-2} (44 000 mmol h^{-1} g^{-1}) which is smaller than that of H: ZnO NRA films. The improved hydrogen production rate for H: ZnO NRA films could be attributed to their ordered structure thereby providing a large accessible surface area for photocatalytic reactions. The ordered H: ZnO structure also forms surface electric fields between NRs that could reduce the recombination of photo-excited electrons and holes, as has been reported for other ordered nanostructures[56]. Several other ZnO based materials like ZnO/TNTs (TiO_2 nanotube arrays)[57], ZnO/g-C_3N_4(ref 58), ZnO –Bi_2S_3(ref 59), reduced graphene oxide (RGO)- ZnO hollow sphere [60], ZnO-CdS[61] have also been explored.

The crystallinity has a marked effect on the photocatalytic activity of the materials synthesized, and thus there has been dedicated research towards the high yield synthesis of many kind of highly crystalline metal oxide and mixed oxide nanocrystals preferably with different morphologies including belt, rod, truncated-octahedron, cubic, sphere, sheet etc. A simple method involving the reaction of inorganic precursors in aqueous solution under hydrothermal conditions has been successful in yielding large quantities of crystalline oxides. A variety of

highly crystalline inorganic nanocrystals can be synthesized in large scale. The shape of inorganic nanocrystals such as $CoWO_4$, $La_2(MoO_4)_3$ can be controlled by adjusting the synthetic conditions including pH and reaction temperature. Usually, the synthesis is carried out in the presence of bifunctional 6-aminohexanoic acid (AHA) as a capping agent where the amine group of AHA ligand gets bonded to the surface of oxide nanocrystals and uncoordinated carboxylic acid group of AHA ligand captures metal ions by its interaction with –COOH group and favors the formation of highly dispersed metal on the oxide surface during the synthesis[62].

Under aqueous conditions, (pH ~ 7.5), noble-metal precursor cations strongly adsorb on the negatively charged surface of 6- aminohexanoic acid-stabilized oxide nanocrystals through electrostatic attraction, due to the deprotonation of –COOH groups. This technique leads to the preferential heterogeneous nucleation and growth of metal precursors on the surface of the substrate seeds via the interaction between noble-metal precursor and uncoordinated carboxylic group of AHA-capped oxide nanocrystals followed by reduction using $NaBH_4$. This leads to high dispersion of tiny metal particles on the nanosupport for the synthesis of a variety of hybrid metal/oxide nanocrystals. Ag/TiO_2 nanobelts have been synthesized as a typical hybrid photocatalyst sample and studied for its photocatalytic activity for methylene blue degradation [63].

The valence and conduction band of semiconductor oxides should have appropriate potentials which can lead to the generation of photoexcited electrons (e^- and holes (h+)). The ease of migration of photoexcited electrons and holes to the surface of the catalyst material is equally important for the fast reduction and oxidation of surface-adsorbed dye/organic moiety. New materials are being explored and examined continuously for facilitating photocatalytic degradation of organic waste and water splitting[64-66]. Tantalates are one such class which evolved owing to the position of the conduction band consisting of 5d orbitals located at a more negative potential than that of titanates (3d) and niobates (4d). The lower potential of the conduction band is advantageous towards the photocatalysis reactions. Among others $Sn_2Ta_2O_7$, $BaTa_2O_6$, $K_3Ta_3B_2O_{12}$, and $NiTa_2O_6$ are the ones which contain Ta^{5+} and have been studied for photocatalytic water splitting under UV light irradiation[67-70].

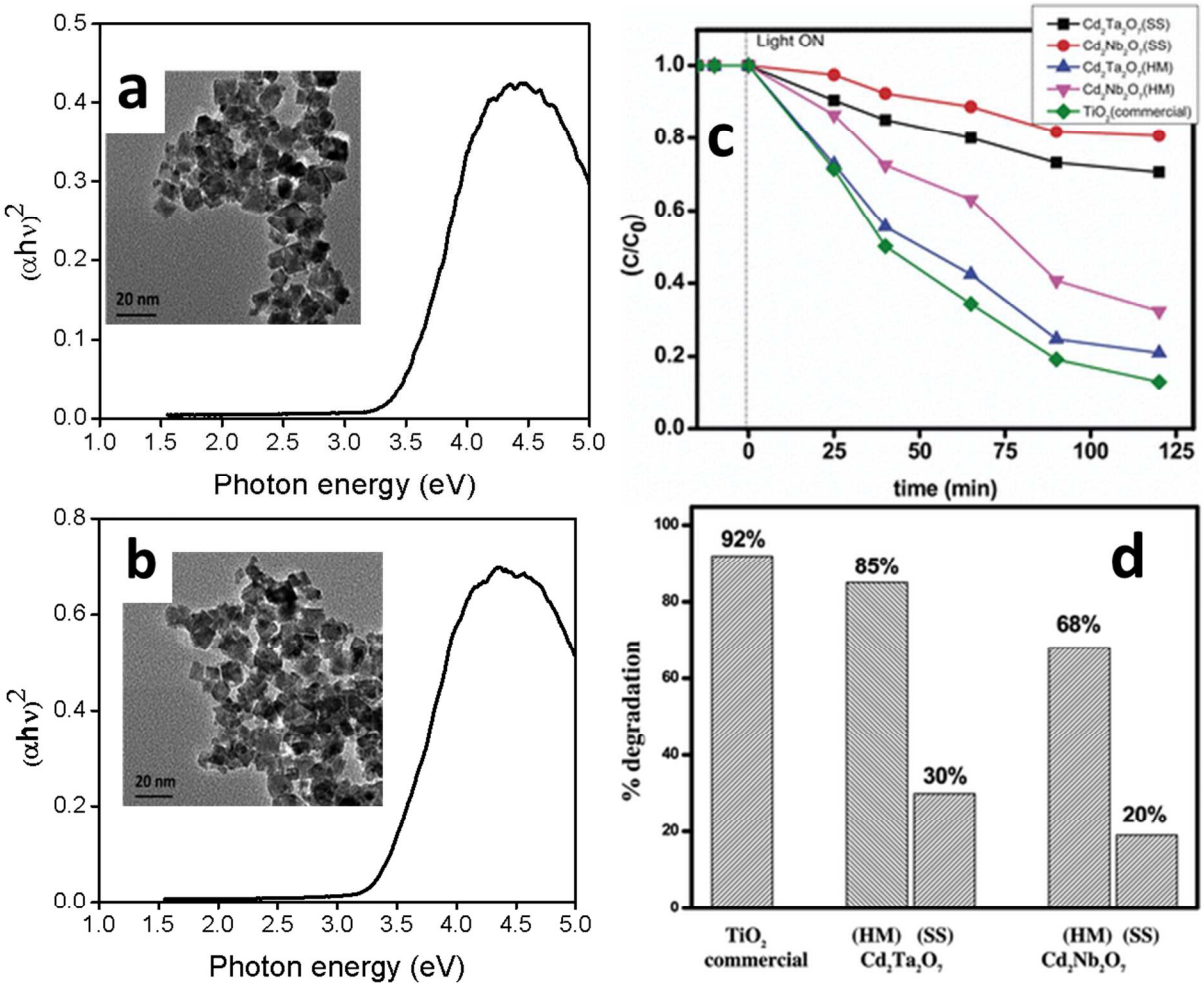

Figure 3. Diffuse reflectance studies of (a) $Cd_2Ta_2O_7$ (inset TEM image of $Cd_2Ta_2O_7$ nanocubes) and (b) $Cd_2Nb_2O_7$ (inset TEM image of $Cd_2Nb_2O_7$ nanocubes). **(c)** Photocatalytic degradation of Rhodamine B using $Cd_2Ta_2O_7$ and $Cd_2Nb_2O_7$ nanocubes at pH 8.5 with O_2 purging. SS (solid state route); HM (hydrothermal method). (d) bar diagram of dye degradation activity of commercial TiO_2, $Cd_2Ta_2O_7$ and $Cd_2Nb_2O_7$. These figures have been reproduced from Ref. 71 with permission from The Royal Society of Chemistry.

The structure of the photocatalyst is very crucial for the smooth migration of electron–hole pairs. Tantalates with corner-shared TaO_6 octahedra possess Ta–O–Ta bond angles close to 180 degree and this accounts for the easy migration of photogenerated electron–hole pairs in the corner-shared framework of TaO_6 units[64, 72]. Tantalates and niobates crystallize in the ABO_3 (perovskite) or $A_2B_2O_7$ (pyrochlore) structure where the B–O–B bond angle is close to 180º. Tantalates and niobates have been synthesized by conventional solid state route or the polymer

precursor method at high temperature (typically 1000–1300 ºC)[73, 74] which results in larger particle size, segregation of components and possible loss of stoichiometry due to volatilization of the constituents. To avoid these, low-temperature, wet chemical routes have been employed to prepare homogenous nano sized particles with higher purity and crystallinity which would eventually enhance photocatalytic activity[75-77]. Influenced by the crystallinity, size, surface charge and surface area, the photocatalytic performance of $Cd_2Ta_2O_7$ and $Cd_2Nb_2O_7$ nanocubes (figure 3a & b) synthesized by hydrothermal route is nearly 7 times more efficient than samples synthesized by solid state route and nearly comparable degradation rate of photocatalysis with commercial TiO_2 [71]. Fig. 3c shows the degradation plot for Rhodamine B in the presence of $Cd_2Ta_2O_7$ and $Cd_2Nb_2O_7$ nanocubes synthesized by hydrothermal and solid state method at pH 8.5 under O2 purging. The rate of photocatalytic activity was significantly higher under basic pH (8.5) with continuous purging of oxygen during the irradiation. Absence of oxygen or lower pH (4.5) decreased the photocatalytic efficiency. The extent of adsorption of dye on the surface of catalyst is partially responsible for this. From the zeta potential measurements, the surface charge on $Cd_2Ta_2O_7$ and $Cd_2Nb_2O_7$ nanocubes was found to change from negative to positive on changing the pH to 4.5 from pH of 8.5. Under basic conditions, the surface of the catalyst is negatively charged and the dye adsorbed easily on the catalyst surface (Rhodamine B being a cationic dye) leading to increase in the rate of photocatalysis. In acidic media, both Rhodamine B molecules and catalyst surface are positively charged and owing to the strong electrostatic repulsion between the similarly charged surfaces, Rhodamine B molecules are less likely to adsorb on the $Cd_2Ta_2O_7$ and $Cd_2Nb_2O_7$ nanocubes. Lower dye adsorptions leads to lower dye degradation which has been studied earlier in case of TiO_2 and Mo doped TiO_2[78]. Fig 3d displays the photocatalytic efficiency of $Cd_2Ta_2O_7$ and $Cd_2Nb_2O_7$ and it was observed that nanocubes synthesized by hydrothermal method is more efficient than the one via the solid state route. In addition, $Cd_2Ta_2O_7$ nanocubes synthesized by hydrothermal route almost comparable degradation rate of photocatalysis with commercial TiO_2

1.2 Composite based photocatalysts

Silica-supported tantalum oxide (ST) hollow spheres were designed for photocatalytic applications in the UV range of 4.1 to 4.8 eV and also to combine the efficient adsorption characteristics of mesoporous silica with the photocatalytic properties of Ta_2O_5 [79]. The design of

these nanostructures enables a good interface between the SiO_2 and Ta_2O_5, which leads to close proximity of the adsorbed dye and the active site of Ta_2O_5 on the silica surface. The synthesis process to obtain these nanostructures is simple and can be obtained by the hydrothermal treatment of tantalum isopropoxide and tetraethylorthosilicate at 120 °C for 48 h in the presence of cetyl trimethyl ammonium bromide, which was used as a capping agent. The maximum observed surface area was found to be 610 m^2/g and pore size distribution of ST hollow spheres varied from 13.4 to 19.0 nm. Lewis acidity of silica and the contact area between SiO_2 and Ta_2O_5 plays a crucial role in controlling the photocatalytic properties of the ST hollow spheres.

Figure 4. (a) shows the TEM images of different SiO_2-Ta_2O_5 samples as synthesized under hydrothermal conditions and also after calcining the samples at 550 °C for 5 h. From TEM studies, an increase in both the shell roughness and thickness was observed after calcinations which could be attributed to the evaporation of leftover aqueous or organic part. Photocatalytic degradation of Rhodamine B was monitored by the dye absorbance at 546 nm as a function of irradiation time in presence of different ST samples (fig 4b) and a remarkable enhancement (~ 6 times) in the photoactivity of silica-supported tantalum oxide hollow spheres was observed when compared to pure Ta_2O_5.

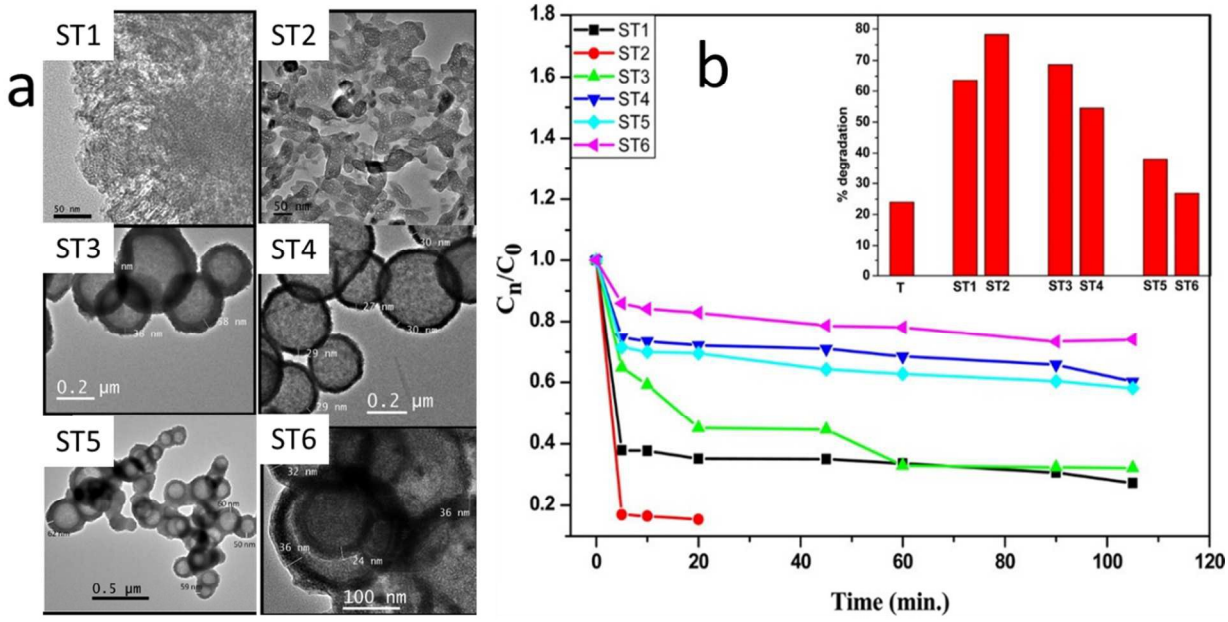

ST1, ST2 (Si:Ta mole ratio = 1:0.1); ST3, ST4 (Si:Ta mole ratio = 1:0.85); ST5, ST6 (Si:Ta mole ratio = 1:1.7).

Figure 4. (a) TEM images of different SiO_2-Ta_2O_5 samples (ST1, ST3, ST5) as synthesized under hydrothermal conditions and (ST2, ST4, ST6) SiO_2-Ta_2O_5 calcined at 550 °C for 5 h. (b) Photocatalytic degradation of Rhodamine B monitored by the dye absorbance at 546 nm as a function of irradiation time in presence of different ST samples. Reproduced from Ref. 79 with permission from The American Chemical Society

The quest for an efficient visible light catalyst leads scientists to develop composites with materials like silica, graphene, graphitic carbon nitride etc. Silver based photocatalysts are very popular in these categories owing to its significantly higher photocatalytic performance[80] than the other known visible light photocatalysts, such as g-C_3N_4, N-doped TiO_2 and $BiVO_4$[81, 82].
But the poor photostability of silver salts limits its extensive use as a visible light photocatalyst. A challenging task thus remains to develop a simple and effective technology which will not only reduce Ag consumption for a Ag_3PO_4 based photocatalyst but will also improve its stability and surface area for large scale applications. Hence, the need of a material with high thermal and chemical stability which can be mixed with the active photocatalyst so as to improve its properties. Graphitic carbon nitride (g-C_3N_4) is one of the π-conjugated semiconductor materials possessing good photocatalytic activity for hydrogen production from water splitting and the photodegradation of organic pollutants under visible light irradiation[83, 84]. The metal free g-C_3N_4 photocatalyst is characterized by a very high thermal and chemical stability, as well as electronic properties but the photocatalytic performance of g-C_3N_4 is still limited due to the high recombination rate of the photo-induced electron–hole pair. Thus modifications are essential to make g-C_3N_4 a valuable material for visible light photocatalysis: one among others is loading of a co-catalyst onto the surface of g-C_3N_4.

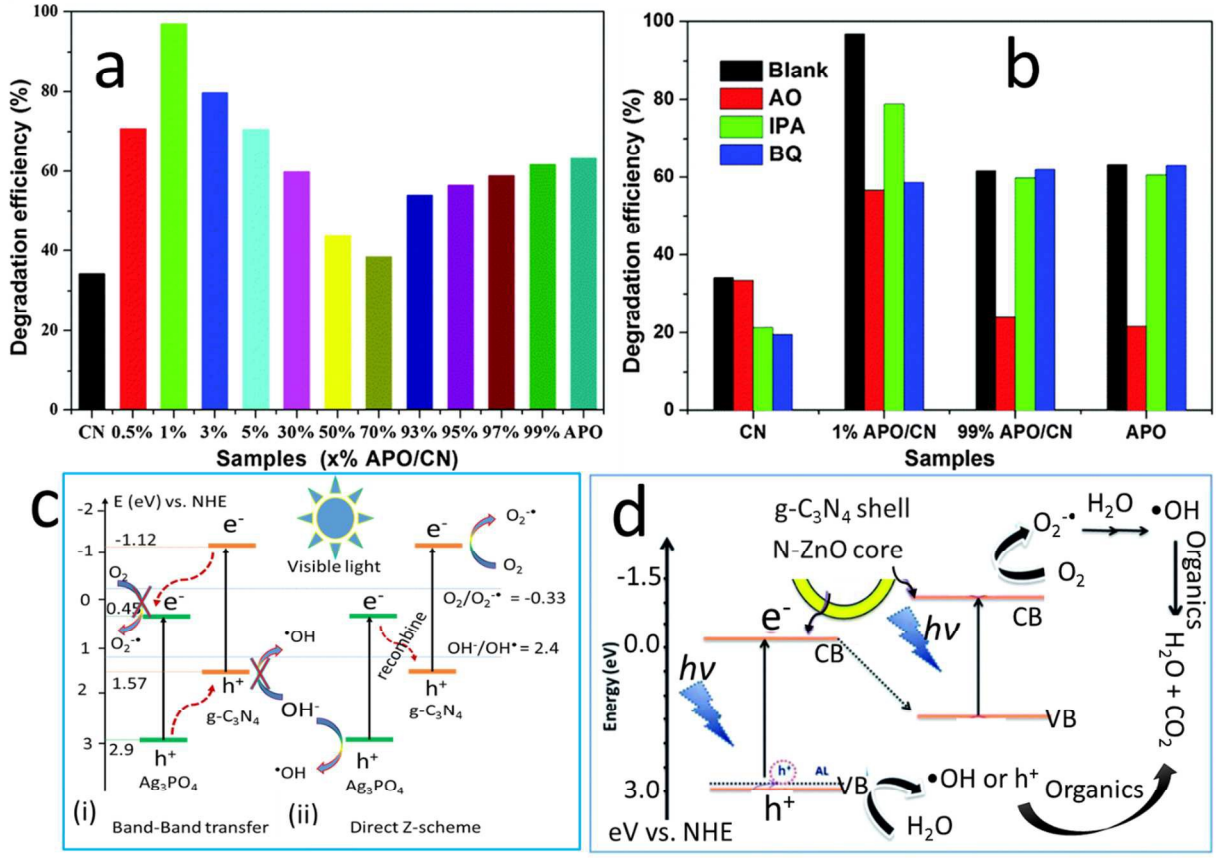

Figure 5. Photocatalytic performances of g-C_3N_4 based composites. (a) Degradation of MB under visible light irradiation for 30 min over different Ag_3PO_4-g-C_3N_4 composite photocatalysts. (b) Effects of a series of scavengers (ammonium oxalate (AO), isopropanol (IPA) and benzoquinone (BQ)) on the MB degradation over different photocatalysts (the dosage of scavengers = 0.1 mmol L^{-1}, irradiation time t = 30 min). Schematic diagram of photoinduced electron–hole transfer processes (c) Ag_3PO_4-g-C_3N_4 composite, band-band transfer and direct Z-scheme transfer. These figures have been reproduced from Ref. 85 with permission from the PCCP Owner Societies and (d) N-doped ZnO/g-C_3N_4 core–shell (Z-scheme transfer) reproduced from Ref. 86 with permission from The Royal Society of Chemistry.

The hybridization of g-C_3N_4 with Ag_3PO_4 led to an enhanced activity under visible light irradiation[87]. The synergic effect between Ag_3PO_4 and g-C_3N_4 led to a structural stability for silver phosphate, high separation efficiency owing to the well positioned C.B. & V.B. positions, The photoinduced electrons in g-C_3N_4 can move freely towards the surface of the Ag_3PO_4 while the holes can transfer to the VB of g-C_3N_4 conveniently and vice versa, since band edges of both g-C_3N_4 and Ag_3PO_4 lie in the visible region. Therefore, g-C_3N_4 can act both as an electron

acceptor and donor. Hence, the electrons can easily migrate to the surface of Ag_3PO_4 and the redundant electrons on Ag_3PO_4 can also be transferred to g-C_3N_4 which separates the electron-hole efficiently. The uniform dispersion of silver nanoparticles onto g-C_3N_4 and the adsorption capacity towards the organic pollutant also contributes to its photocatalytic efficiency.

The optimum photocatalytic activity of g-C_3N_4–Ag_3PO_4 at 25 wt% of g-C_3N_4 under visible light is almost 5 and 3.5 times higher than pure g-C_3N_4 and Ag_3PO_4 respectively. On similar lines were designed N-doped ZnO/g-C_3N_4 hybrid core–shell nanoplates via a facile, cost effective and eco-friendly ultrasonic dispersion method. The direct contact of the N-doped ZnO surface and g-C_3N_4 shell without any adhesive interlayer, introduced a new carbon energy level in the N-doped ZnO band gap thereby effectively lowering the band gap. The synergistic effect at the interface of the N-doped ZnO and g-C_3N_4 results in increased area of exposure, energy band structure and enhanced charge separation. Consequently, the hybrid core–shell nanoplates exhibit enhanced visible-light photocatalysis towards the degradation of Rhodamine B in comparison to that of pure N-doped ZnO and g-C_3N_4. These studies show the importance of evaluating new core–shell composite photocatalysts with g-C_3N_4 as shell material[86].

To promote the separation of photoinduced electron-hole pairs by the effective transfer of photogenerated electrons and holes at the interface, TiO_2 based nano-heterostructures[88a, 88b] have been synthesized. The attachment of visibly active photocatalytic nanoparticles on the TiO_2 surface has been found to enhance the photocatalytic activity in both the UV and visible regions[89]. On similar lines, ceria/ titania heterostructures have been designed which were found to exhibit an enhanced broad light wavelength region of photocatalytic activities of CeO_2 /TiO_2 nanobelt heterostructures. Under UV irradiation, both TiO_2 and CeO_2 can be excited, which results in the generation of photo generated holes in the valence band (VB) and electrons in their conduction band (CB).

CB electrons (CeO_2) easily migrate to the CB of TiO_2 through the interface, because the conduction band-edge potential of CeO_2 (−0.3 eV) is more negative than that of TiO_2 (−0.27 eV). Similarly, because the valence band-edge potential of CeO_2 (2.42 eV) is lower than that of TiO_2 (2.88 eV), VB holes (TiO_2) can inject to the VB of CeO_2 by the control of the interface. This separates the photoinduced electron-hole pairs in TiO_2 and CeO_2 thereby improving photocatalysis. Whereas under visible light irradiation, the electrons in the VB CeO_2 are excited

to its CB. The photogenerated electrons in the CB of CeO_2 can be transferred to the CB of TiO_2, leading to efficient charge separation[90].

Also the matching band energy between CeO_2 nanoparticles and TiO_2 nanobelts facilitates the separation of photoinduced electron-hole pairs and the higher surface area of CeO_2 nanoparticles on the surface of TiO_2 nanobelts results in a strong capture of MO molecules which facilitates the faster degradation. Many such composites have been designed like TiO_2 with graphene[91] and also with reduced graphene[92]. Water-dispersible, core-shell magnetic nanoparticles of Fe_3O_4@TiO_2 have been synthesized by anchoring cyclodextrin cavities to the TiO_2 shell. The tethered cyclodextrins are responsible for the dispersibility of the nanoparticles in aqueous medium. The amorphous TiO_2 shell is the photocatalyst for the degradation and mineralization of the organics, bisphenol A and dibutyl phthalate, under UV illumination, and the magnetism associated with the 9 nm crystalline Fe_3O_4 core assists in the magnetic separation[93].

The fabrication of type II heterostructures plays an important role in modification of photocatalysts and has been extensively studied. He el al. have discussed applications in the area of environmental remediation and water splitting[94].

Our group has also been extensively working on photocatalysis in order to design effective photocatalysts. Along with advantages of ZnO & TiO_2, are the associated disadvantages like the fast recombination rates of electrons & holes resulting in the low quantum efficiencies thereby limiting the photocatalytic activity. The second and most important factor lies in its inability to utilize the visible range of the solar spectrum which limits their use. With these limitations in mind, photocatalytic systems were designed with chemical potential gradients by creating heterojunctions which assist in the localization of the electron and holes at two different sites in the catalyst. Narrow/mid band gap semiconductor nanocrystals have also been used as a sensitizer to enhance the visible light absorption thereby increasing their activity. CdS[95], CdSe[96], PbS[97], Bi2S3[98], InP[99], Ag2S[100] are some of the visible light photocatalysts that are being used as a sensitizer. In addition, geometric constraints on the materials were also found to be an effective way of limiting the electron-hole recombination. One dimensional ZnO nanostructures have been an ideal choice for an effective electron transport which limits the recombination rate. To understand the efficacy of the separation of electron and hole in anisotropic material Type II ZnO/ CdS core shell nanorod array with varying shell thickness has been synthesized[101]. The coupling of the two semiconductors led to enhanced light absorbing capacity & is characterized

by longer lifetime, higher activity & enhanced current than pure ZnO & CdS thereby indicating that type II core shell structures are efficient for photocatalytic & PV application. The dye degradation studies using these core shell nanorod array were found to be highly dependent on the shell thickness (figure 6d).

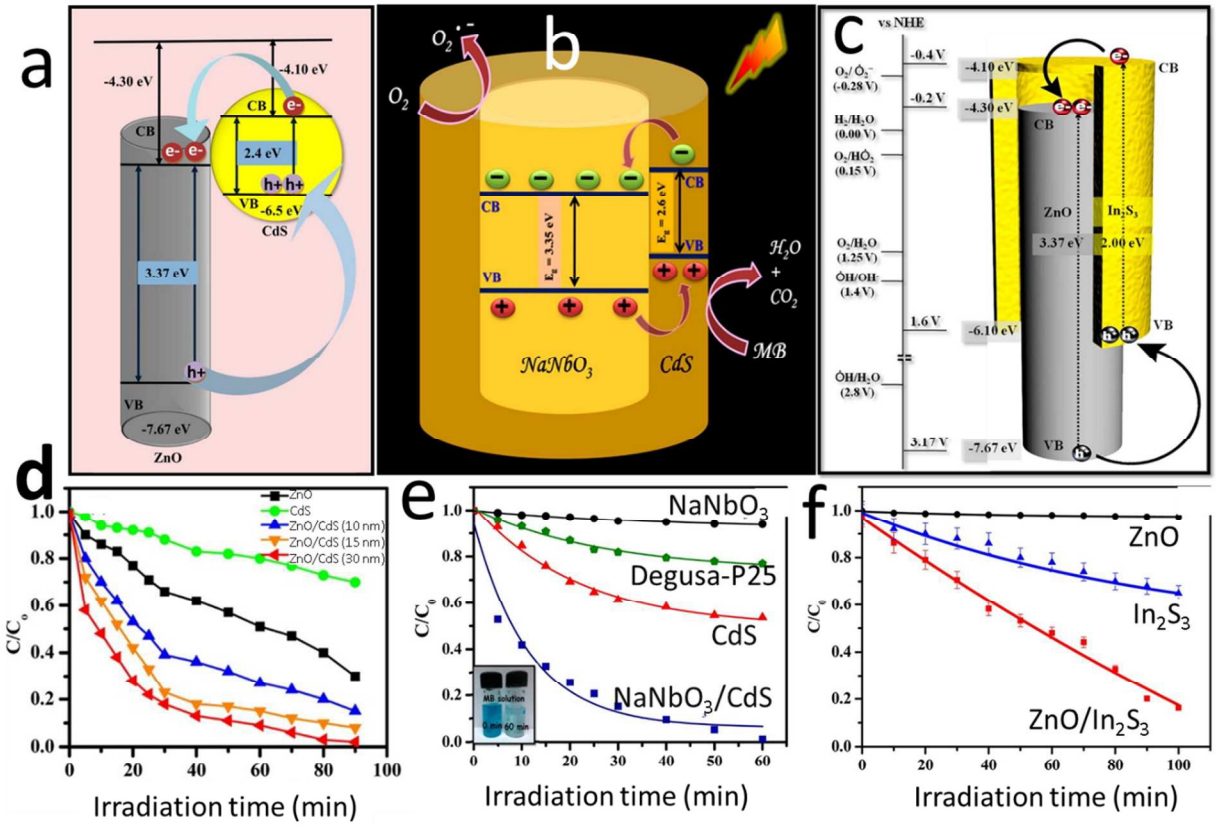

Figure 6. Schematic diagram of the core/shell nanorod arrays, showing the type-II band gap alignment: electron–hole pair generation by incident photons and electron injection from the excited shell material into the metal oxide core. (a) ZnO-CdS core-shell , (b) $NaNbO_3$-CdS core- shell and (c) ZnO-In_2S_3 core-shell. Photocatalytic dye degradation monitored by the C/Co Vs. time plot in presence of different core-shell photocatalyst (d) ZnO-CdS, (e) $NaNbO_3$-CdS and (f) ZnO-In_2S_3. Figure a and d were reproduced from Ref. 101 with permission from The American Chemical Society, Figure b and e has been reproduced from Ref. 102 with permission from The American Chemical Society, Figure c and f have been Reproduced from Ref. 103 with permission from The American Chemical Society.

In another case study (Type II semiconductor), core-shell nanostructures of ZnO@In_2S_3 led to effective injection of photogenerated electrons from In_2S_3 into ZnO which increased the probability of absorption of radiation in the visible range. These results reveal that the

combination of narrow band gap with wide band gap semiconductor enhances their photocatalytic abilities to a greater extent i.e. ~ 5 times higher than In_2S_3 nanoparticles and 56 times higher than ZnO nanorods [103].

Figure 6 (a-c) shows the schematic diagram of the core/shell nanorod arrays, showing the type-II band gap alignment: electron–hole pair generation by incident photons and electron injection from the excited shell material into the metal oxide core and fig 6(d-f) shows the photocatalytic dye degradation monitored by the C/Co Vs. time plot in presence of different core-shell photocatalysts (a) ZnO-CdS, (b) $NaNbO_3$-CdS and (c) ZnO-In_2S_3 respectively.

In addition to core-shell nanostructures of two semiconductors, heterostructures have also been studied to extend the photo response of ZnO. Semiconductors with narrow band gap like CdS, PbS, In2S3 and Bi2S3 have been attached on the ZnO surface to make suitable heterojunctions (band gap engineering) and these heterostructures can function in visible light as photocatalyst[104-106]. CuS is a narrow band gap semiconductor (2.2 eV) and is a very suitable candidate for visible light photocatalysis without any toxic element[107, 108]. Type-II semiconductor with p-n heterojunction has been fabricated by decorating CuS nanostructure on the surface of ZnO nanotubes[109]. These ZnO/CuS heterostructures efficiently decompose methylene blue upon irradiation of visible light in room temperature. The percentage of degradation being 0.6, 63 and 87% for ZnO, CuS and ZnO/CuS respectively after irradiation of visible light in 30 min . The rate constant 'k' for pure CuS is 9.8×10^{-3} min^{-1} whereas when ZnO/CuS has been used as photocatalyst the value of 'k' increases three times to 2.3×10^{-2} min^{-1}. Efficient adsorption of dye molecules on the catalyst surface and successive decomposition of the dye molecule by reaction with the photogenerated electron and hole seperately.[28] In this case hierarchical morphology of the ZnO/CuS heterostructures and the negative surface charge of the sample leads to enhanced adsorption of the cationic dye methylene blue on the catalyst surface. There are other reports where metal nanoparticles like Ag[110], Au[111], Pt[112] have been decorated on the surface of ZnO, to delay the recombination rate of the photo generated electrons and increase the efficiency of ZnO.

2. Nanostructured metal oxides and their hybrids for electrocatalytic (HER, OER and ORR) applications

Metal oxides are one of the most enthralling classes of inorganic solids with diverse structures, properties and applications. Metal oxides find applications in microelectronics, sensors, piezoelectric devices, phosphors, coatings, fuel cells, energy storage/conversion devices, coatings and catalysts[113-115]. Electro catalysis is a combination of principles of electrochemistry and catalysis whereby the presence of an electro catalyst enhances the rate of electrochemical reaction at anode or cathode[116, 117]. The origin of electro-catalysis was in early 1920s when Bowden and Riedel measured the rate of hydrogen evolution reaction (HER) on several metals[118, 119]. Development of electro catalysts is gaining lot of importance as several energy technologies depend upon electrochemical reactions. We have discussed here the fundamental understanding and advances of HER, OER and ORR activity studies of nanostructured metal oxides and their hybrid materials as electro catalysts. The dependence of electrocatalytic activity on size, facet, surface area, core/ shell of nanometal oxides and the strong interaction between carbon supports with metal oxides are discussed thoroughly. Here we confine to the recent literature pertaining to HER, OER and ORR by nanostructured metal oxides and their hybrid materials.

2.1 Hydrogen evolution reaction (HER)

Hydrogen as a fuel has several advantages due to high combustion heat, zero pollution and plentiful natural abundance. Study of Hydrogen evolution reaction (HER) allows one to understand the fundamentals of electrode kinetics as well as improving the hydrogen production through water electrolysis[120]. Hydrogen evolution reaction (HER) is the cathode half reaction in which H_2 is evolved during water splitting. It is a reverse reaction to hydrogen oxidation reaction (HOR) and both involve only two electron transfer leading to kinetically fast reaction unlike oxygen evolution reactions (OER) / oxygen reduction reactions (ORR) which involve four electron transfer and are kinetically sluggish. According to the widely accepted mechanism, HER at a metal electrode in acidic medium involves three steps[121, 122]. The first step (Volmer or discharge step) involves the generation of surface adsorbed hydrogen (H_{ads}) through the coupling of single electron transfer at the interface with proton to the surface. After the generation of H_{ads}, it can follow two paths: one could be recombination of two surface adsorbed H atoms to generate

H_2 by desorption (Tafel step) or the other way is by protonation of H_{ads} (Heyrovsky step) coupled to a single electron transfer[121, 122].

$$H^+_{(aq)} + e^- \rightarrow H_{ads} \quad \text{(Volmer (or) discharge step)} \quad 4a$$

$$2\,H_{ads} \rightarrow H_2 \quad \text{(Tafel step)} \quad 4b$$

$$H_{ads} + H^+_{(aq)} + e^- \rightarrow H_2 \quad \text{(Heyrovsky step)} \quad 4c$$

As can be seen from above reactions, the strength of M-H_{ads} interaction plays important role in deciding the activity of electro-catalyst. If the Volmer reaction is the rate determining step (RDS), the resulting Tafel curve should yield a slope 118 $mVdec^{-1}$. While if Heyrovsky step is the RDS, the measured Tafel slope would yield a value of about 40 mV dec^{-1} (or) 30 mV dec^{-1}.

The above three steps of HER(4a-c) should satisfy thermodynamic constraints[123] and if we assume reactions follow Volmer- Heyrovsky mechanism,

$$E^o_{H+/Hads} + E^o_{Hads,\,H^+/H2} = E^o_{H+/H2} = 0 \quad (5)$$

For Volmer reaction (4a) the equilibrium potential of the redox reaction for an adsorbed or chemisorbed state can be considered as

$$\Delta G(H_{ads}) = \Delta G(H^+ + e^-) \quad (6)$$

According to Norskov et al[124], $\Delta G(H^+ + e^-)$ is 0 at E = 0 (vs NHE) and $-e_oE$ at any other potential E. The electrosorption valency corresponding to equation (6) is close to 1 and static dipole moment of the H_{ads} bonded to the surface is close to zero. Hence for Volmer reaction the standard equilibrium potential can be written as

$$E^o_{H^+/Hads} = -\Delta G^o/(H_{ads})/e_o \quad (7)$$

$\Delta G^o(H_{ads})$ is the adsorption energy of H_{ads} and if $\Delta G^o/(Hads) < 0$, H_{ads} formation on catalyst surface is thermodynamically favorable, $E^o_{H^+/Hads} > 0$.

$$E^o_{H+/Hads} = -E^o_{Hads,\,H^+/H2} < 0 \quad (8)$$

For HER at E = 0, H_{ads} formation is thermodynamically favorable and molecular hydrogen formation should be thermodynamically unfavorable. For this situation, the thermodynamic overvoltage η_T can be written as

$$\eta_T = E^o_{H^*,\,H_{ads}/H_2} - E^o_{H+/H2} \quad (9)$$

The above step which is thermodynamically least favorable step is termed as the potential determining step (not kinetically rate determining step). As the lowest possible $\eta_T = 0$, a catalyst with following condition need to be designed:

$$\eta_T = E^o{}_{H^+/Hads} = E^o{}_{Hads,\ H^+/H2} = G^o/(Hads)/e_o = 0 \qquad (10)$$

When the above analysis follows Volmer-Tafel mechanism for HER/HOR and standard equilibrium constant of reaction can be written as

$$K_{Hads/H2} = \exp(-\Delta G^o(H_{ads})/RT \qquad (11)$$

In such a case,

$$E^o{}_{H+/Hads} - \Delta G^o/(H_{ads})/e_o = 0 \qquad (12)$$

As per Heyrovsky-Volmer mechanism, thermodynamic over voltage $\eta_T = E^o{}_{H+/Hads}$ in case of $E^o{}_{H+/Hads} < 0$. For the case of $E^o{}_{H+/Hads} > 0$, the Tafel reaction becomes endothermic and potential determining.

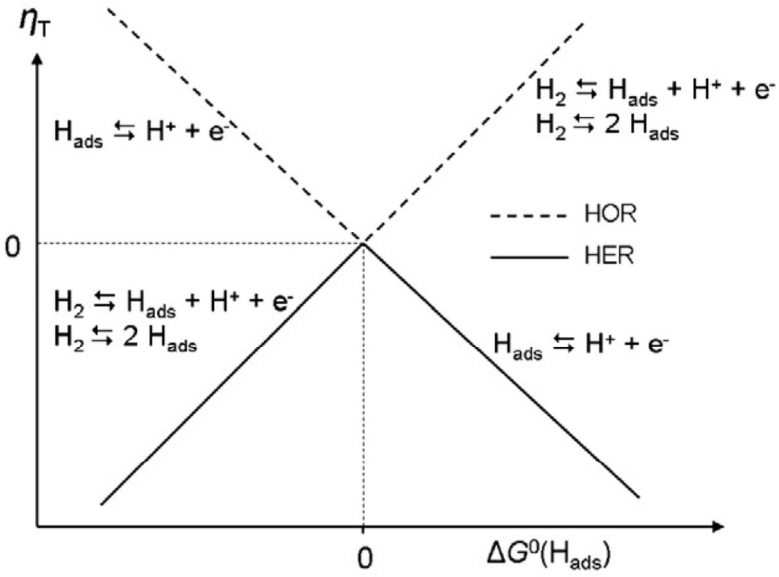

Figure 7. ‘‘Thermodynamic” volcano plot for the hydrogen evolution reaction (HER) and the hydrogen oxidation reaction (HOR): thermodynamic overpotential (standard equilibrium potential of the potential-determining step) vs. the free binding energy of hydrogen on the electrode surface. The dashed-line gives the same plot for the HOR. The potential-determining steps corresponding to the various legs of the curves are indicated. Reproduced from the ref. 123 with permission of Elsevier.

As can be seen from the Volcano plot (Figure 7), η_T for the HER as a function of $G^o/(H_{ads})$ and illustrates how the optimal catalyst is a compromise between strong and weak binding of H_{ads}. For the reduction reaction ∨- shaped plot and for oxidation reaction ∧- shaped plot were observed. Based on above considerations, the best catalyst for HER is the one that binds in such a way that there is no sink or barrier in going from reactant to product through an intermediate.

Three important parameters play a crucial role in selecting catalytically active HER catalysts. The material should possess intrinsic electrocatalytic effect, large active surface area per unit volume ratio and good electrochemical stability. Platinum which is a noble metal and platinum based alloys are the most effective catalysts for HER with small over potential. However the high cost, scarcity and CO poisoning of Pt based materials are the limitations for their HER based applications. Recently more economical non-noble metal based HER electrocatalysts have been explored such as transition metal chalcogenides, carbides, oxides although they are less effective and stable than Pt based electrocatalysts[122]. Here we focus on the recent studies concerning the nanostructured metal oxides for HER study.

Tungsten oxide (WO_3) is known to form tungsten bronze (H_xWO_3) which is a good electron and proton conductor and hence is a promising electro-catalyst. Luo and coworkers demonstrated the effect of Ta^{5+} doping on HER activity of WO_3 nanowires. They prepared Ta-doped WO_3 nanowires by hydrothermal method and observed that compared to undoped samples, Ta doped ones exhibit two times higher current density; Ta-doped WO_3 nano wires (10.72 mA cm^{-2}) and undoped WO3 (5.34 mA cm^{-2}) at an over potential of -0.52 V. The best HER performance was achieved with molar ratio of Ta/W being 0.01. With the addition of Ta^{5+} in WO_3 it creates more defects or oxygen vacancies such that more protons are intercalated which enhances electron transfer to improve the HER activity[125].

Atta et al[120] prepared $ARuO_3$ (A = Ca, Sr or Ba) nanoparticles (40-100nm) by co-precipitation method. The HER activity of as studied by Tafel polarization is in the order of $BaRuO_3$> $CaRuO_3$> $SrRuO_3$. The exchange current density values observed were, -60.7, -13.1 and -884.6 μA cm^{-2} and activation energy values 42.6, 86.3 and 17.7 kJ/mol for Ca, Sr and $BaRuO_3$, respectively. The A site metal ion in perovskite plays important role on the stability of crystal structure as well as improves catalytic activity through synergistic interactions with B-site metal ion. In $BaRuO_3$, Ru-Ru bond length is much less compared to Ca or Sr compounds, indicating strong Ru-Ru bonding, leading to enhanced HER activity. When ternary oxides like $Sr_{1-x}Ca_xRuO_3$ were prepared, they exhibit increased activity than binary oxides more so with Ca doping[121]. Layered misfit compounds are popularly known for their thermoelectric properties, while misfit oxide like $Ca_3Co_4O_9$ prepared by Pumera and co-workers was known to be a highly active electrocatalyst for both HER and ORR studies. In HER activity $Ca_3Co_4O_9$ electrode surface gave a Tafel slope of 87mV/decade, compared to glassy carbon electrode (130

mV/decade). $Ca_3Co_4O_9$ exhibits higher heterogeneous electron transfer rate of 3.76×10^{-4} cm s^{-1} compared to 3.11×10^{-4} cm s^{-1} for glassy carbon. Even though inferior in its efficiency, due to its lower cost and affordability it is very good alternative for Pt[126]. Yamada et al investigated the effect of size and shape of a series of Co_3O_4 nanoparticles on H_2 evolution by ammonia-borane (AB) hydrolysis. Although the size effect is minimal, there is a dependence on the shape. Among cube, hexagonal sheets and irregular particles, the hexagonal sheet was observed to show highest activity. The rate of hydrogen evolution for Co_3O_4 sheet was 0.35 mmol/min in between 5 and 10 min and for cube, 0.22 mmol/min. Even though cubic particles were small with high surface area sheet morphology exhibits pronounced H_2 evolution due to atom alignment on surface. In the sheet, the (211) plane where Co atoms are aligned at large distances while for cube it is (100) plane with atoms aligned in close packed form. Cu loading in Co_3O_4 decreases the induction period (0.5% Cu-6 min. 4% Cu- 0.7 min) and increases the rate of H_2 evolution to 0.63 mmol/min[127].

NiO/Ni/CNT heterostructures (Figure 8a) have been found to be highly effective electrocatalyst for hydrogen evolution[128]. These heterostructures were synthesized by thermal decomposition (at 300 °C, Ar atmosphere) of $Ni(OH)_2$ bonded with carbon nanotube (CNT) surface. NiO/Ni heterostructures were characterized using XPS and XANES studies (Figure 8b, c). Incomplete coverage of Ni core by NiO exposes the Ni/NiO interfaces which are synergistically active HER catalysis in alkaline medium (Figure 8d). In alkaline medium, OH^- ions from water splitting gets attached electrostatically on the NiO surface at the Ni/NiO interfaces due to Ni^{2+} species. Two mechanisms are possible for HER in alkaline medium as given below.

$H_2O + e \rightarrow H_{ads} + OH^-$ (Volmer) and

$H_{ads} + H_{ads} \rightarrow H_2$ (Tafel)

Or

H2O + e $\rightarrow H_{ads} + OH^-$ (Volmer) and

$H_2O + H_{ads} + e \rightarrow H_2 + OH^-$ (Heyrovsky)

At the interface, nearby Ni sites facilitates Volmer process (H adsorption) and imparts the synergistic effect of Ni/NiO interfaces in HER whereas only NiO does not show HER catalysis as it lacks H adsorption sites[128].

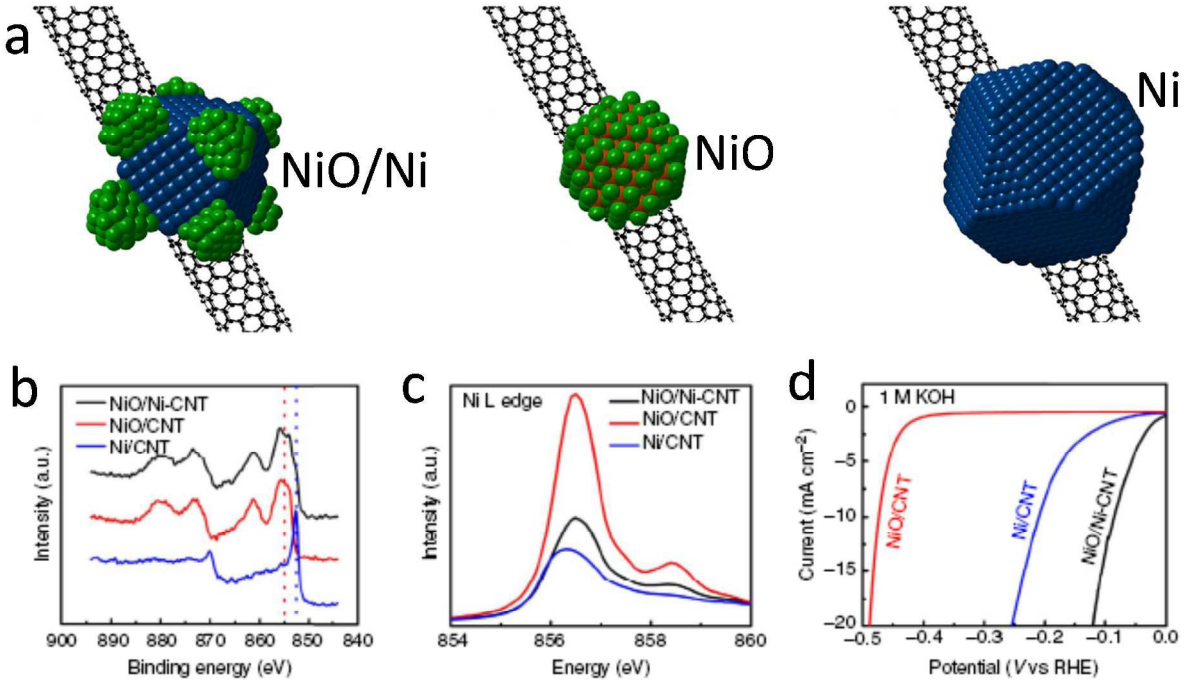

Figure 8. (a) Schematic of NiO/Ni-CNT, NiO/CNT and Ni/CNT structure. (b) High-resolution Ni XPS spectra of the three hybrid materials (the dotted line points out the binding energy of Ni2þ (red) and metallic Ni (blue). (c) Ni L edge XANES spectra of the three hybrid materials. (d) Linear sweep voltammetry of the three hybrid materials in 1M KOH at a scan rate of 1mV/s under the loading of 0.28 mg cm^{-2} on RDE showing superior HER catalytic activity of NiO/Ni-CNT. Reproduced from the ref. 128 with permission of Nature publishing group.

Novel RuO_2/Ni nano/microarchitecture was fabricated to study the HER activity. Compared to pure RuO_2, p-Ni (p = porous) and Ni, RuO_2/p-Ni catalyst is known to exhibit high HER activity. At larger current densities (> 40 mA cm^{-2}), the RuO_2/p-Ni composite leads to superior HER performance than the Pt catalyst. The high HER activity of composite is attributed to incorporation of RuO_2 into porous Ni structure which has large specific surface area. The synergistic effect results in enhanced activity with hydrogen spillover as well as it improves the long term durability of catalyst[129].

Ganguli and co-workers have investigated the HER and OER performance of Cu metal NPs (4-6nm) synthesized from aligned copper oxalate nanorods which were prepared by microemulsion method. Controlled decomposition of oxalate nanorods under Ar atm. results in the synthesis of crystalline, uniform nanoparticles with high surface area. The hydrogen evolution reaction (HER) study of Cu NPs resulted in current density of 12 mA cm^{-2} (on GCE) and 46 mA cm^{-2} (Pt

electrode) which were significantly higher than reported values (maximum 1 mA cm^{-2}). The catalyst has shown very good stability. In case of HER it was stable even after 50 cycles. The enhanced activity and good stability were attributed to small size NPs with high surface area (34 m^2 g^{-1})[130]. Ganguli and co-workers described the effect of low temperature synthesis of Cu-Cu_2O and their HER, OER photocatalytic properties. Copper oxalate nanorods and CuO (1:1) precursors were annealed in Ar atm. at 350°C leading to 25nm size particles and around 100nm NPs of Cu_2O were obtained when CuO alone without oxalate precursor were annealed at 850°C. The NPs obtained at 350°C were known to show better HER activity than those obtained at 850°C. The HER current densities were found to be 0.0207 cm^2 mg^{-1} & 0.0235 cm^2 mg^{-1} for GC electrode and 0.0324 cm^2 mg^{-1} & 0.0476 cm^2 mg^{-1} for Pt electrode for Cu_2O obtained at higher and lower temperature respectively. As shown in the figure 9, the current density was found to be 14 times higher than GC and 4 times higher than Pt electrodes for Cu_2O synthesized at 350°C compared to 850°C. They also show stability up to 50 cycles. The enhanced activity of NPs obtained at 350°C is related to their small particles size and high surface area[131].

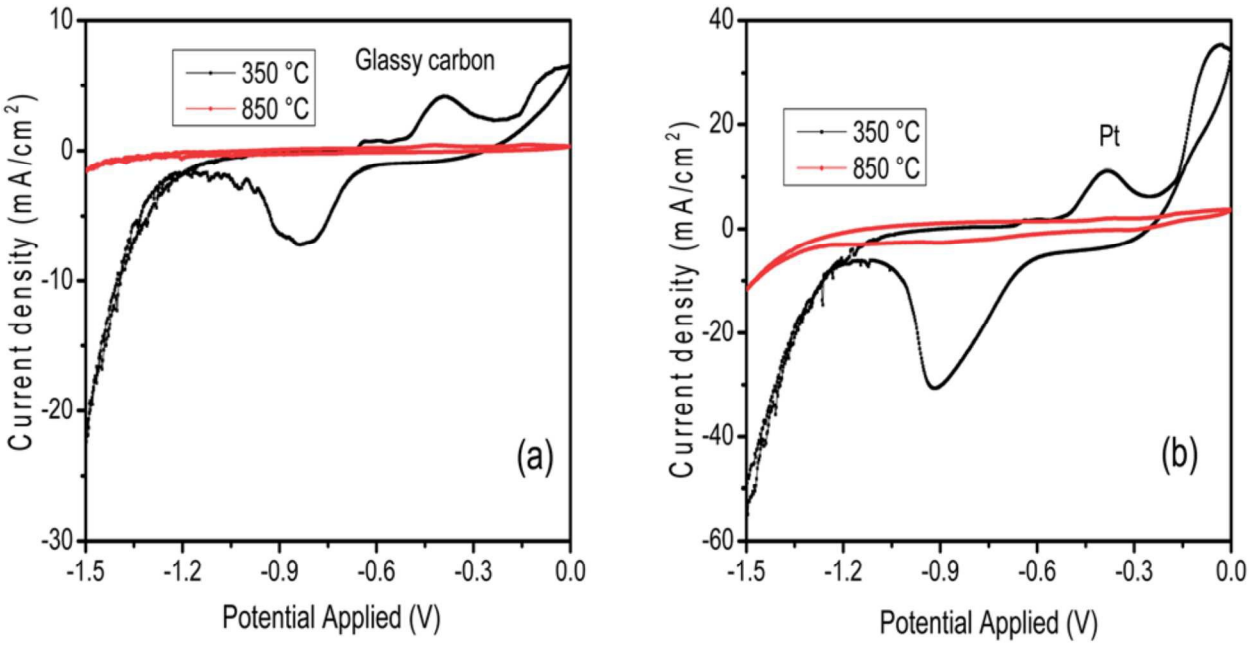

Figure 9. HER of Cu_2O synthesized at different temperature (a) on glassy carbon and (b) platinum as working electrode. Reproduced from the ref. 131 with permission of the Royal Society of Chemistry.

2.2 Oxygen evolution reaction (OER)

Oxygen evolution reaction (OER) is an anodic half-cell reaction in which oxygen is evolved in the electrochemical oxidation of water during water splitting or solar cells and metal air batteries . It is the reverse reaction to oxygen reduction reaction (ORR), both processes being kinetically sluggish and involves multi step proton coupled electron transfer. Before going into examples of metal oxides studied, we discuss the mechanism of OER involving these electrocatalysts. Chemical composition, electronic structure and surface atomic arrangement of the electrocatalyst influences the OER performance. As OER is very sensitive to the surface, the thickness and morphology of oxide layer play an important role[122]. One of the proposed mechanisms of OER involves the coordination of water to the metal oxide surface with subsequent proton transfer to solvent and electron transfer to the electrode to form M-OH species (equation 13) and then M-O species is formed via proton coupled oxidation (equation 14) or by disproportionation M-OH (equation 15) . The M-O species liberates O_2 by decomposition of bimolecular species decomposition (equation 16) or by the attack of water (hydroxide) (equation 17). The sequence of reactions involved are shown below[121].

$$M + H_2O \rightarrow MOH + H^+ + e^- \quad (13)$$

$$MOH \rightarrow MO + H^+ + e^- \quad (14)$$

$$2MOH \rightarrow MO + M + H_2O \quad (15)$$

$$2MO \rightarrow 2M + O_2 \quad (16)$$

$$MO + H_2O \rightarrow M + O_2 + 2H^+ + 2e^- \quad (17)$$

Sabatier's principle[132] indicates that OER activity depends on the bond strength of the catalyst surface and reactant/product. Ideally moderate bond strength, neither too strong nor too weak are useful. Apart from noble metals and noble metal oxides (RuO_2 & IrO_2) the search is on for an efficient metal oxide electrocatalyst with low cost, stability in strong alkaline media, environment friendly and most importantly one that can lower the overpotential to sustain appreciable current. RuO_2 and IrO_2 are the most widely studied OER catalysts in acidic or alkaline media but are expensive and thus a low cost oxide electrocatalysts with high activity and durability is desired. A large variety of oxides of Fe, Mn, Ni and Co including simple oxides such as Fe_3O_4, MnO_2, NiO and Co_3O_4 and several mixed metal oxide spinels and perovskites have been recently explored for their OER activity[133]. Our group has reported OER activity of ternary metal oxide like Mg_2MnO_4 and $NiCo_2O_4$ nanostructures[134, 135] in alkaline medium (Figure 10). The nanorods of smallest particles having highest surface area shows higher OER

activity[135]. The morphology dependent OER activity of nickel cobaltite ($NiCo_2O_4$) has also been explored. These nanostructures with three different morphologies such as square sheet, hexagonal sheet and spherical particles were prepared by solvothermal method. Hydrolyzing agent (urea or NaOH or NH_4OH) plays an important role in controlling the morphology. Among the three samples as shown in Figure 10b, the square sheets were found to exhibit highest OER activity with current density of ~280 mA/cm^2. The highest activity of square sheet of $NiCo_2O_4$ was attributed to high surface area (100 m^2 g^{-1}), (larger pore volume (0.227 cm^3 g^{-1}) and ordered pore distribution[136].

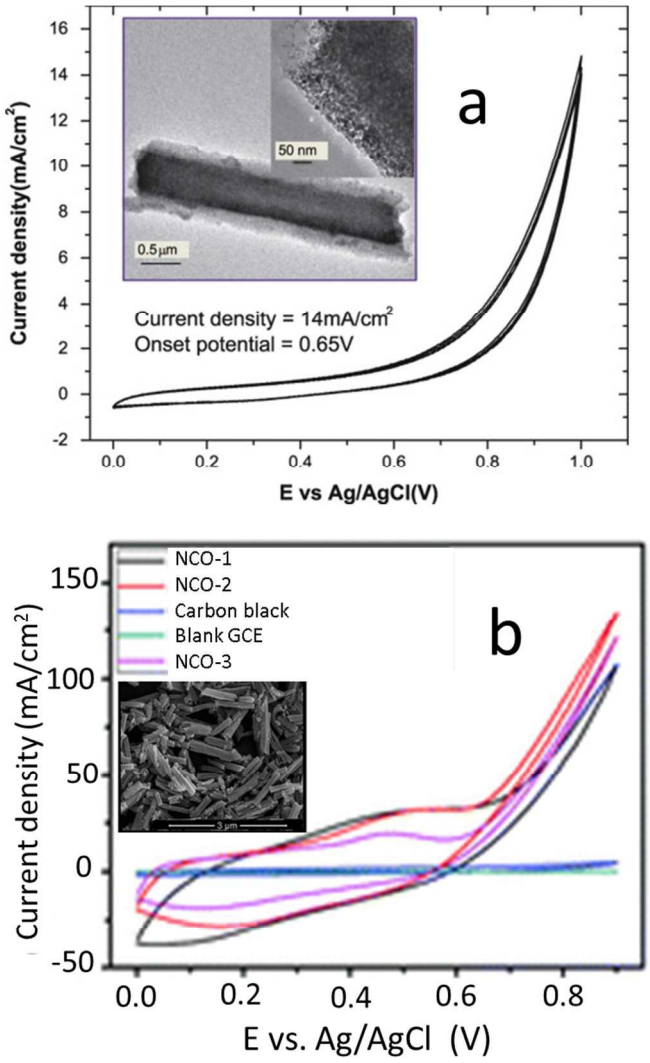

Figure 10. (a) Cyclic voltammogram of Mg_2MnO_4 nanostructure (inset TEM micrograph of Mg_2MnO_4). Reproduced from the ref. 134 with permission of Elsevier. (b) Cyclic voltammograms of $NiCo_2O_4$ (different aspect ratio NCO-1, 2 and 3) towards the oxygen evolution reaction. Reproduced from the ref. 135 with permission of the Royal Society of Chemistry.

A detailed study on the synthesis of anisotropic Co_3O_4 nanostructures with controlled morphology for OER activity has been reported[137]. There Co_3O_4 nanoparticles were obtained from various types of cobalt oxalate precursors. The rate of decomposition of the precursor was vital in getting particles with different sizes and aspect ratio (Figure 11a). Among the Co_3O_4 nanoparticles, the ones obtained at 300°C showed highest current density (104 mA/ cm^2) at an onset potential around 0.38 V, while for NPs obtained at 400, 500, and 600 °C the onset potential was recorded at 0.43, 0.45, and 0.58 V, respectively to r same current density (Figure 11b). The difference in particle size and aspect ratio of nanorods were key in obtaining high current density. For the Co_3O_4 nanostructures obtained at 300°C, had the highest aspect ratio 10.5:1 and each rod consisted of very tiny particles with average size of 8−10 nm and these nanostructures lead to high OER[137].

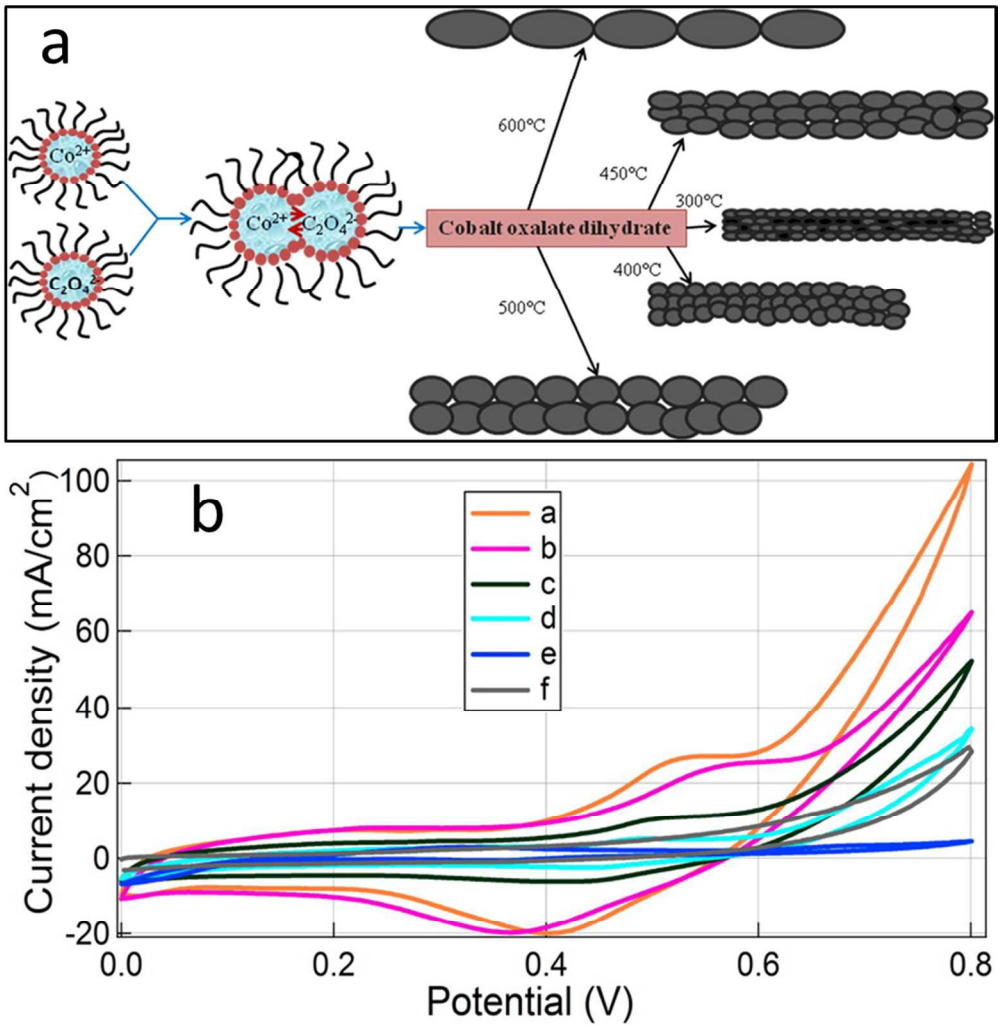

Figure 11. Anisotropic assembly of Co_3O_4 nanoparticles. (a) Schematic diagram for the growth process of Co_3O_4 nanorods. (b) Cyclic voltammograms of Pt working electrode loaded with Co_3O_4 nanostructures obtained at different temperatures: (a) 300, (b) 400, (c) 500, and (d) 600 °C, (e) bare Pt, and (f) Pt with carbon. Reproduced from the ref. 137 with permission of American Chemical Society.

Molecular orbital calculations have been attempted to predict the enhanced OER activity observed among the perovskite structure of type $A_{1-x}A'_xB_yB'_{1-y}O_3$, where A or A′ is a rare-earth or alkaline-earth metal and B or B′ is a transition metal. The OER activity of these oxides showed a volcano type dependence. Among the several oxides studied, $Ba_{0.5}Sr_{0.5}Co_{0.8}Fe_{0.2}O_{3-d}$ (BSCF) is predicted to show highest OER activity[138]. The OER activity was predicted at an e_g occupancy close to unity, with high covalency of transition metal oxygen bonds.

Chen and coworkers developed a novel and simple room temperature methodology to prepare nanocrystalline spinels $M_xMn_{3-x}O_4$ (M = divalent metals like Co, Mg, Zn, etc.). They used reduction-recrystallization approach with MnO_2 nanoparticulate as the starting material. The resulting spinels $Co_xMn_{3-x}O_4$ had definite morphology and controlled crystal phase either as cubic or tetragonal. As electrocatalysts, nanoparticles obtained at ambient conditions normally outperform the high temperature synthesized powders for ORR and OER activity. The enhanced performance of nanoparticles is attributed to high specific surface area and abundant defects. Among cubic and tetragonal phases, the latter is known to exhibit twice the OER activity due to the dissimilar binding energies of oxygen adsorption on cobalt and manganese defect sites. For ORR activity it is the cubic Co–Mn–O spinel which outperforms the tetragonal phase[139].

Very recently, Alejandra Ramírez et al prepared homogeneous thin films of three different manganese oxides, α-Mn_2O_3 (mostly Mn III), MnOx (Mn III, IV) and Mn_3O_4 (Mn II, III) by Galvanostatic anodic deposition on F: SnO_2/glass and were annealed at different temperatures to improve crystallinity[140]. The oxygen evolution in 1M KOH of these oxides for onset at an overpotential (η) of 170 mV vs. RHE (at J = 0.1mA/cm^2) the current densities of 20 mA/cm^2 at η =230 mV vs. RHE for α-Mn_2O_3, (at J = 0.1 mA/cm^2) with current densities of ca. 20 mA/cm^2 at η = 290 mV vs. RHE for MnO_x (at J = 0.1 mA/cm^2) and current densities of ca. 10 mA/cm^2 at η = 570 mV vs. RHE for Mn_3O_4 were observed. The highest OER activity of α-Mn_2O_3 is related to its crystal structure and compared to other oxides it exhibits a very short O-O distance of 2.55 Å which facilitates the O_2 generation. One more advantage observed for α- Mn_2O_3 was its low specific resistivity owing to which it has a fast recharge capacity than other manganese oxides.

Mn_3O_4 phase shows semi covalent nature in tetrahedral sites and ionic character in octahedra which hinders the O_2 evolution compared to α-Mn_2O_3 [140].

McCrory et al evaluated the oxygen evolution activity of the following oxides: CoO_x, CoP_i, $CoFeO_x$, NiO_x, IrO_x, $NiCeO_x$, $NiCoO_x$, $NiCuO_x$, $NiFeO_x$, and $NiLaO_x$ in acidic and alkaline solutions. They observed that all the non-noble metal catalysts exhibit similar OER activity in 1 M NaOH, achieving 10 mA cm^{-2} current density at overpotentials between 0.35 and 0.43 V (Figure 12). The IrOx catalyst achieved 10 mA cm^{-2} current density at η = 0.32 ± 0.04 V under similar conditions although it was unstable during 2h of constant current electrolysis. Among all these oxides studied, $NiFeO_x$ stands out due to its lower surface area and hence higher specific activity; at η = 0.35 V, it also has specific current density 10 times higher than other non-noble metal catalysts studied[141].

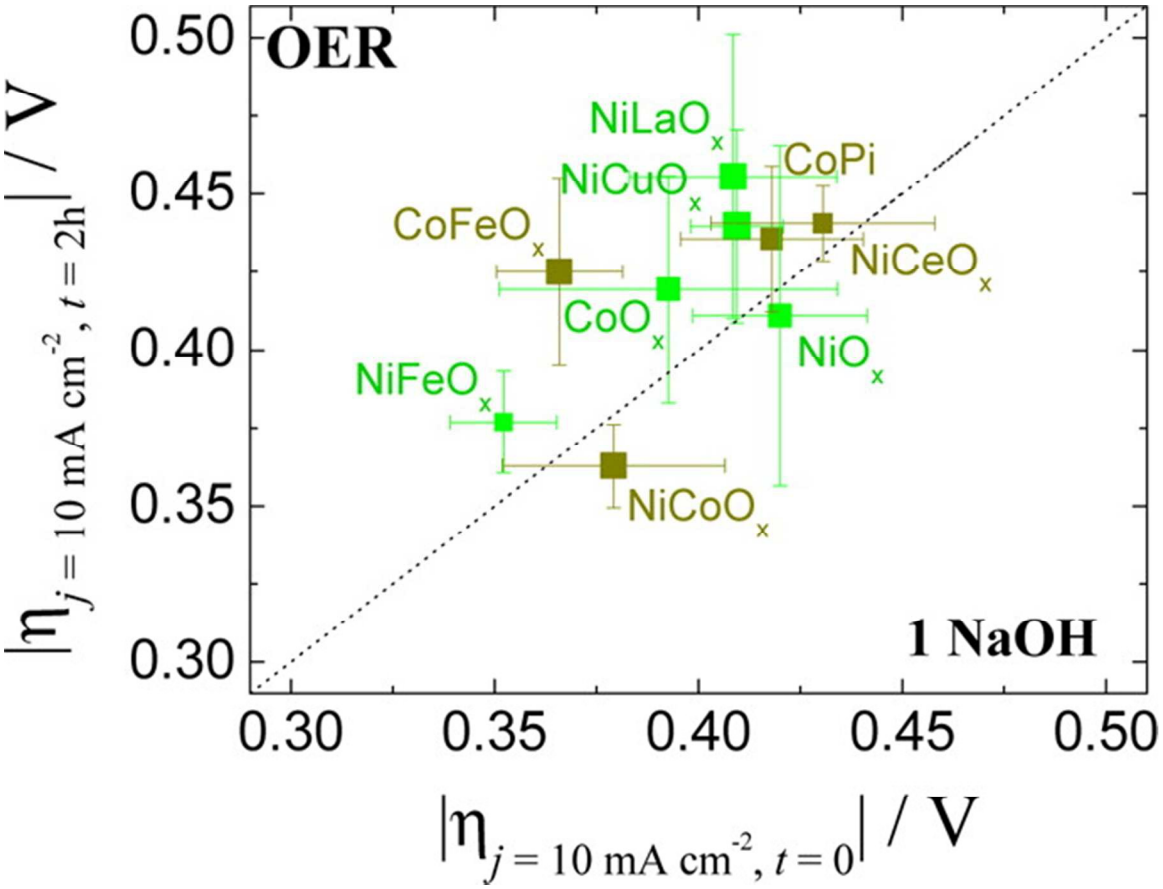

Figure 12. Zoomed-in region of interest for alkaline OER from Figure 6. The x-axis is the overpotential required to achieve 10 mA cm−2 per geometric area at time t = 0. The y-axis is the overpotential required to achieve 10 mA cm^{-2} per geometric area at time t = 2 h. The diagonal dashed line is the expected response for a stable catalyst. The color of each point represents the roughness factor of the catalyst with a bin size of 1 order of magnitude. Reproduced from the ref. 141 with permission of American Chemical Society.

Manthiram et al studied the role of morphology and surface planes on OER activity in the $LiMn_{1.5}Ni_{0.5}O_4$ spinel. The specific catalytic activities of the truncated octahedra, cubic, spherical, octahedral were 1.1, 1.7, 2.2, and 3.3 mA/cm^2 at 1.7 V vs RHE respectively. Octahedra sample with all {111} surface planes exhibits the highest activity whereas the truncated octahedral sample with {001} surface planes exhibits lowest activity (Figure 13). The Tafel slopes for the cubic, spherical, octahedral, and truncated octahedral samples are, respectively, 120, 73, 70, and 92 mV dec^{-1}. The octahedral sample exhibits the lowest Tafel slope of 70 mV dec^{-1} with highest durability while truncated octahedral sample exhibits the highest Tafel slope of 120 mV dec^{-1} with durability similar to the cubic and spherical samples[142].

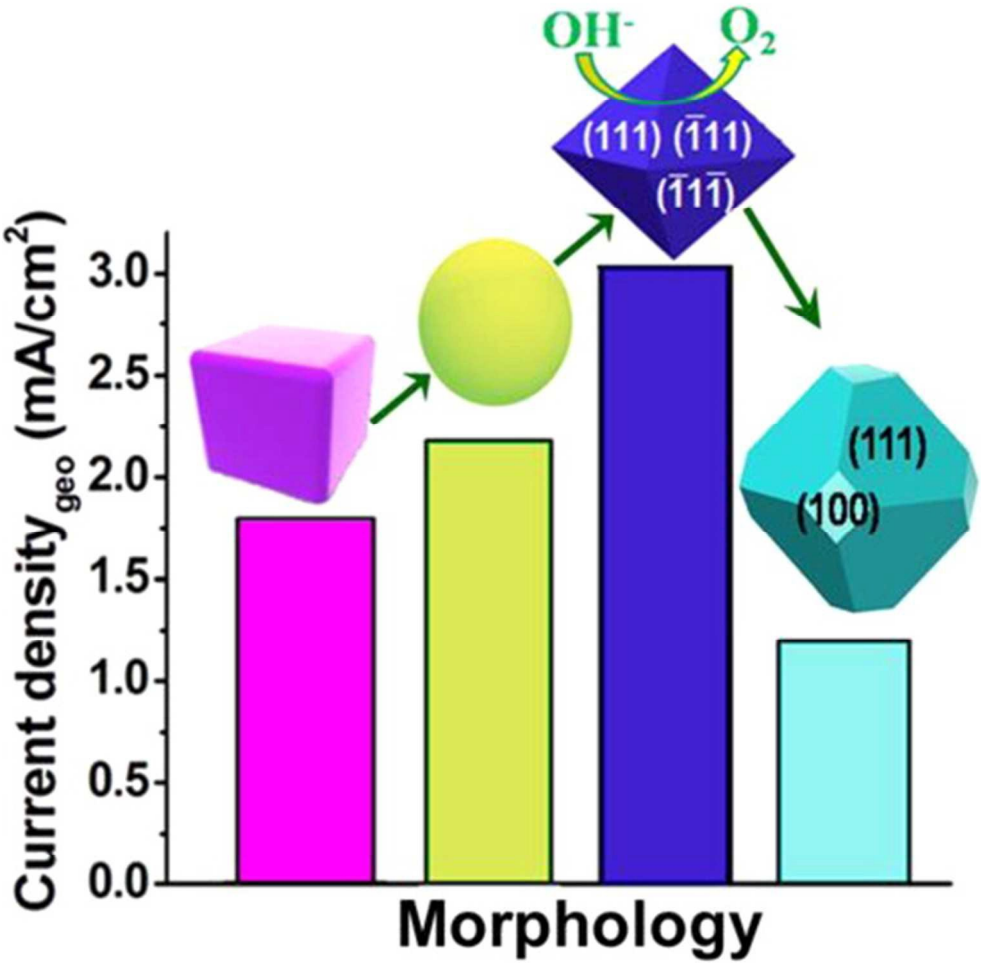

Figure 13. Histogram illustrating the shape-dependent electrocatalytic activity of $LiMn_{1.5}Ni_{0.5}O_4$ spinel oxides for OER. Reproduced from the ref. 142 with permission of American Chemical Society.

Liu et al developed a cost effective scalable method to fabricate hierarchical $Zn_xCo_{3-x}O_4$ nano array structures. These nanostructures have large surface area, high porosity and high active site density. The $Zn_xCo_{3-x}O_4$-1:3 Nano arrays exhibit outstanding OER activity with a small over potential of 0.32 V at a current density of 10 mA/cm^2 with a Tafel slope of 51 mV/decade.

That is how $Zn_xCo_{3-x}O_4$-1:3 nano arrays exhibit superior OER performance than pure Co_3O_4 and a commercial Ir/C catalysts[143]. Chen and Qiao fabricated three dimensional (3D) network of N-doped graphene (NG)-$NiCo_2O_4$ (NiCo) hybrid with hierachial pores as an advanced OER catalysts for water splitting. The materials studied for OER activity are PNG-NiCo, NG-NiCo, PNG, PG-NiCo (PG = porous graphene) exhibit onset potential of 310, 340, 352 mV and 315 mV (LSV) respectively. Among all these, PNG-NiCo shows high activity with small onset potential which is more negative than other samples. PNG-NiCo exhibit excellent current densities of 5 mA cm^{-2}, 21.1 mA cm^{-2} at the over potentials of 373 mV and 564 mV respectively which are comparable to noble metal catalysts. The edges and defective sites of $NiCo_2O_4$ are the active centers to facilitate the dissociation of water. The novel performance of PNG-NiCo is attributed to the very strong interactions between $NiCo_2O_4$ and N-doped graphene which results from the direct growth of $NiCo_2O_4$ on graphene sheets[144]. A novel core-ring $NiCo_2O_4$ nanoplatelets were prepared by simple co-precipitation followed by decomposition at 200°C. The core ring nanoplatelets, thus obtained exhibit better OER performance (an overpotential of 0.315V at a current density of 100 mAcm^{-2}.) than Co_3O_4 or $NiCo_2O_4$ nano particles prepared by other methods. The core ring structure provides exceptionally active surface area with all top and bottom surface of the core ring, side surfaces of the ring as well as core being active for electrocatalytic activity. Core and ring were known to show similar surface $(\bar{1}11)$ plane which has the high Co atom density. Due to the Co rich surface taking part in OER, exchange of electrons is increased between water and $NiCo_2O_4$ core ring nanoplatelets resulting in the apparent current density of electrode catalyst[145].

The incorporation of Cu into Co_3O_4 nanoparticles (NPs) ($Cu_xCo_{3-x}O_4$, $0 < x < 1$) by thermal decomposition and its effect on OER performance was studied by Wu and Scott[146]. $Cu_xCo_{3-x}O_4$ NPs with an average particle size of 20-30nm crystallize in cubic spinel structure. Among all the samples studied, $Cu_{0.7}Co_{2.3}O_4$ was known to exhibit high current density of 1 A cm^{-2} at a voltage of 1.8V in 1 mol dm^{-3} KOH at 25^{o}C. Cu incorporation shifts the $Co^{3+/}Co^{4+}$ redox peak, onset potential of OER to more negative values. One more reason attributed for high OER is inversion

of Cu^{2+} into the octahedral sites leading to more Co^{3+} occupying the tetrahedral sites, which influences the surface properties as well as improved OER activity[146].

Dual phase (mixed cubic and tetragonal) nanocrystals of $MnCo_2O_4$ spinels (dp-$MnCo_2O_4$) were prepared by simple hydrothermal method[147]. These were integrated with nanocarbon materials like N-rGO and CNT. The coupled materials act as bi-functional catalysts, exhibiting superior OER activity with respect to commercial Pt/C. Mechanically mixed dp-$MnCo_2O_4$ + CNT mixture exhibits inferior electrocatalytic kinetics which shows that strong covalent hybrid coupling between both the components is necessary. In OER activity, the onset potentials of dp-$MnCo_2O_4$/CNT and dp-$MnCo_2O_4$/ N-rGO observed were much lower than Pt/C and current densities observed are much higher than Pt/C. The $MnCo_2O_4$ – nanocarbon hybrids outperformed Pt/C with overall activity and durability in enhanced OER performances due to synergetic covalent coupling phenomena which was observed from binding energy shifts of Co, Mn, C and N with or without spinel/nanocarbon integration[147].

2.3 Oxygen reduction reaction (ORR)

Oxygen reduction reaction (ORR) is a cathode half reaction involving the reduction of oxygen in fuel cells, metal air batteries and chlor-alkali electrolysis. The reduction involves strong O=O bond and it requires four coupled electrons and proton transfers. Hence ORR is kinetically very sluggish. ORR may also proceed through two electron process to hydrogen peroxide, the H_2O_2 formed may further reduce to water or it may catalytically decompose. Oxygen reduction is associated with very high positive potential hence we need materials which can contribute high current without dissoluting themselves. Because of this reason, only noble metals and their alloys are widely studied for ORR[121, 122]. Platinum (Pt) and platinum based alloys are used as catalysts in cathode compartments of fuel cell devices. High cost of Pt due to scarcity and sluggish electron transfer kinetics associated with cathode reaction are the major barriers for the commercialization of fuel cells. Hence there is a great need for the development of non-precious metal based electrocatalysts for ORR in the development of energy conversion devices like fuel cells and metal air batteries[148].

Transition metal oxides, sulphides, carbides or nitrides such as Co_3O_4, Fe_2O_3, Fe_3O_4, MnO_x, TiO_2, NbO_2, Ta_2O_5, Co_9S_8, WC and TiN were extensively studied as active catalysts for ORR. Noble metal catalysts are active for ORR in acidic medium, while non-precious metals based catalysts are active in alkaline medium. Several mixed transition metal oxides such as AMn_2O_4

(A= Co, Ni, Zn) or ACo_2O_4 (A = Mn, Ni, Cu) act as potential candidates due to their high abundance, ease of preparation and outstanding redox stability in aqueous alkaline solutions[147, 149]. Variable valence states of metals and structural flexibility of spinels offer an opportunity to fine tune their catalytic properties. Frequently, the non-noble metals and metal oxide catalysts suffer from dissolution, sintering and agglomeration result in the catalyst degradation during fuel cell operation. To overcome this, metal oxides were combined with nanocarbon species such as graphene, carbon nanotubes (CNT) which themselves by virtue are good ORR catalysts. The combination of metal oxides and nanocarbon improve the electrocatalytic activity, durability and high electrochemical stability due to their excellent conductivity and large surface area. The strong interaction between nanocarbon support and metal oxides is one of the main reasons for enhanced catalytic activity[122, 147, 149].

The dependence of adsorption orientation of oxygen molecules on electrocatalyst surface was explained by El-Deab and Ohsaka. MnO_x nanorods with porous texture were electrodeposited on to Pt electrode to make nano-MnO_x/Pt surface. Compared to bare Pt and MnO_x, the composite is known to exhibit significant positive shift of the onset potential of the ORR. Electronic structure of Pt surface does not change after loading with MnO which means the improved ORR activity does not arise from the change of Pt electronic surface. On bare Pt surface, parallel adsorption of O_2 molecules (one O_2 molecule per one Pt atom) results in zero ring current. However nano-MnO_x/Pt surface have parallel, end on orientation of oxygen molecules. This results in having more oxygen molecules on nano-MnO_x/Pt surface leading to higher ring current, positive shift of ORR onset potential and higher reaction rate [150]. Sun and co-workers prepared Co/CoO coreshell nanoparticles and combined with graphene (G) by self-assembly method. Thus obtained G-Co/CoO composite exhibits comparative activity and better stability than commercial Pt-C. Co core in Co/CO core-shell plays key role in improving the ORR activity. Graphene as a support plays important role in enhancing the ORR performance as G–Co/CoO NPs show a more positive half-wave potential (-0.176 V) than C–Co/CoO NPs (-0.290 V) in O_2-saturated KOH (0.1M) solution. CoO shell thickness also plays an important role i.e. 1 nm thick shell show maximum activity[151]. Retna Raj and coworkers investigated the effect of N-doping in reduced graphene oxide (rGO) on ORR activity for which they made N-rGO-Mn_3O_4 hybrid by simple sonication and reflux method using hydrazine as reducing agent[148]. The onset potential for

oxygen reduction is observed at -0.075 V for N-rGO-Mn_3O_4 hybrid which is 60-225mV less negative than rGO/Mn_3O_4, Pt/C, free Mn_3O_4, and N-rGO/Mn_3O_4 mixture. The current density at potential of -0.6 V for the hybrid is 1.3-2.3 times higher than bare N-rGO and Mn_3O_4. The enhanced ORR activity arises from synergistic effect, as the pyridinic nitrogens present in the hybrid improves the direct reduction pathway for ORR[148]. Zhai et al have grown the $CoMn_2O_4$ spinel nanocrystals on poly diallyldimethylammonium chloride (PDDA) functionalized carbon nanotubes (PDDA-CNTs)[149]. Co_3O_4 on PDDA-CNTs exhibit high ORR activity with onset potential of -0.07V whereas $CoMn_2O_4$/PDDACNTs exhibit much positive onset potential (-0.009 V). The enhanced ORR activity of hybrid is due to the high surface area and abundant defects in $CoMn_2O_4$ along with that in the nitrogen free CNT plane. PDDA creates net positive charge to facilitate ORR activity. The $CoMn_2O_4$/PDDA-CNTs hybrid also exhibit excellent OER activity and durability[149].

Li et al demonstrated the structure dependent ORR activity of Cu_2O nanocrystals[152]. They have used PEG and PVP as capping agents. With PEG, 40nm nanocubes were obtained with dominant {100} plane, as the reaction time increases cubes are truncated to become spheres with more {111} planes. In case of PVP, porous Cu_2O nanocrystals formed with mixed {100} and {111} planes. Even though three Cu_2O samples show same onset potential, the electrocatalytic activity kinetic range varies with different planes as seen from the Tafel slope. The ORR kinetics of Cu_2O nanocrystals is controlled by charge transfer and intermediate migration, these two processes are faster on {100} plane than on {111} plane. The Cu_2O nanocrystals also show better methanol tolerance and durability than commercial Pt/C[152].

The fabrication of 3D monolithic Fe_3O_4 NPs on N-doped graphene aerogels (N-GAs) (Figure 14a) was done by Wu et al[153]. This non-precious metal based hybrid catalyst acts as an efficient ORR catalyst. Fe_3O_4/N-GAs exhibit positive ORR onset potential (−0.19 V) and high current density (−2.56 mA cm^{-2}, Figure 14b) than for Fe_3O_4/N-GSs (−0.26 V, −1.46 mA cm^{-2}) and Fe_3O_4/N-CB (−0.24 V, −1.99 mA cm^{-2}). Fe_3O_4/N-GAs hybrid also has lower H_2O_2 yield, and higher electron transfer number for the ORR in alkaline media than the other hybrids. GA has 3D macropores, interconnected macroporous network for the uniform distribution of Fe_3O_4 NPs and high specific area which are key in enhancing the ORR activity of Fe_3O_4/N-GAs[153].

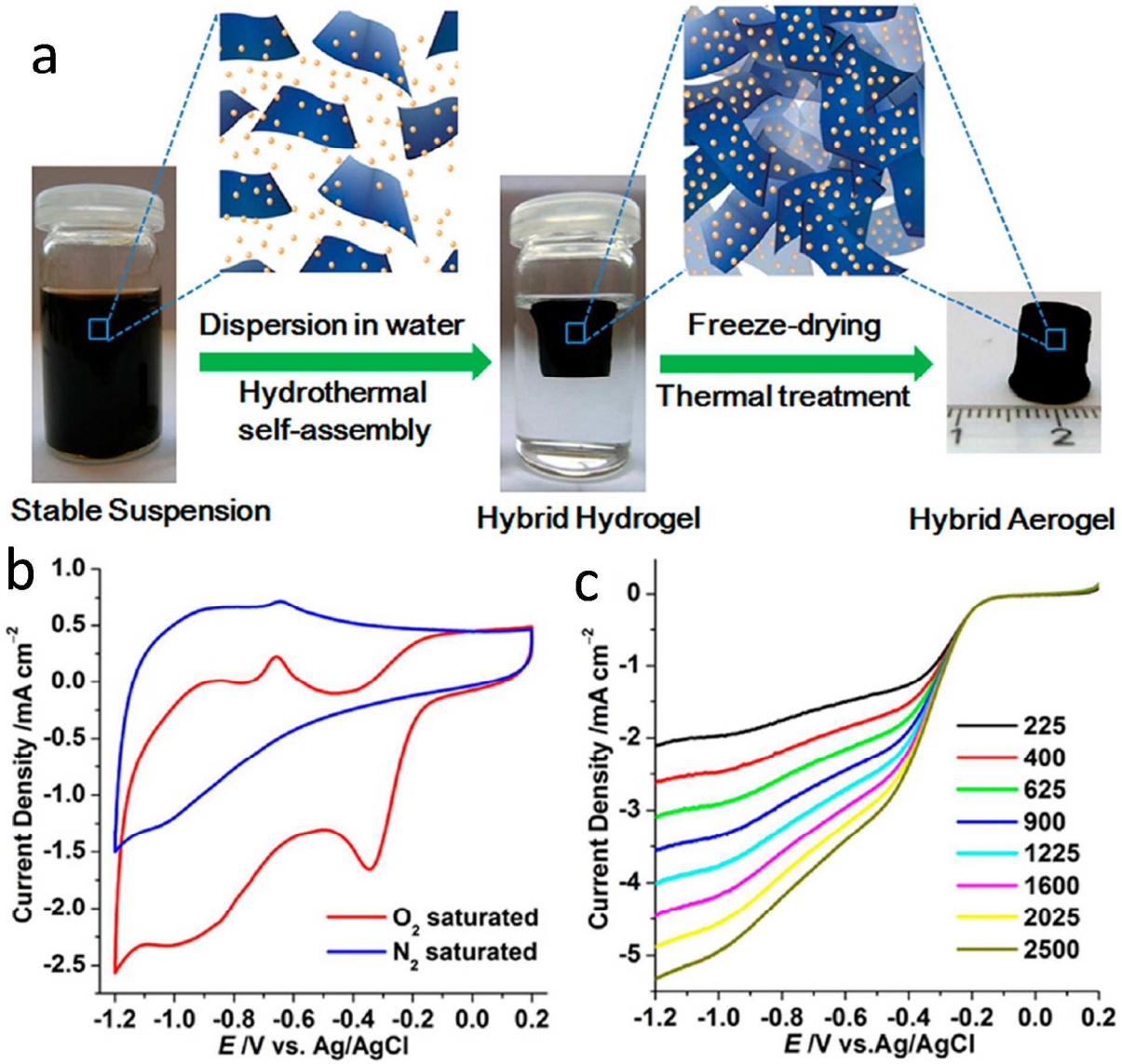

Figure 14. (a) Fabrication process of monolithic Fe_3O_4 NPs supported on 3D N-doped graphene aerogels (Fe_3O_4/N-GAs), (b) cyclic voltammetry of Fe_3O_4/N-GAs in N_2- and O_2-staturated 0.1 M aqueous KOH electrolyte solution at a scan rate of 100 mV s^{-1} and (c) Linear sweep voltammetry of Fe_3O_4/N-GAs in O_2-saturated 0.1 M KOH at a scan rate of 10 mV s^{-1} at different RDE rotation rates (in rpm).Reproduced from the ref. 153 with permission of American Chemical Society.

Liang et al developed a simple strategy to prepare spinel manganese-cobalt oxide ($MnCo_2O_4$)-mildly reduced graphene oxide (N-rGO) covalent hybrid for ORR activity[154]. Compared to Co_3O_4/N-rGO hybrid, the Mn substitution leading to $MnCo_2O_4$/N-rGO increases the activity of catalytic sites of the hybrid materials to boost the ORR activity. In basic medium at 0.7 V vs. RHE, the ORR activity of $MnCo_2O_4$/N-rGO hybrid afforded current density of 151 mA/cm^2 which is 7 times higher than simple mixture of $MnCo_2O_4$ + N-rGO (22 mA/cm^2). The hybrid

exhibits strong covalent interactions as C-O and C-N can form C−O−metal and C−N−metal bonds between metal and N-rmGO. Particle size higher than 10nm of $MnCo_2O_4$ shows poor ORR than 5nm one and the content of $MnCo_2O_4$ (65-80%) afford high ORR, lesser or higher than this will result in poor ORR[154].

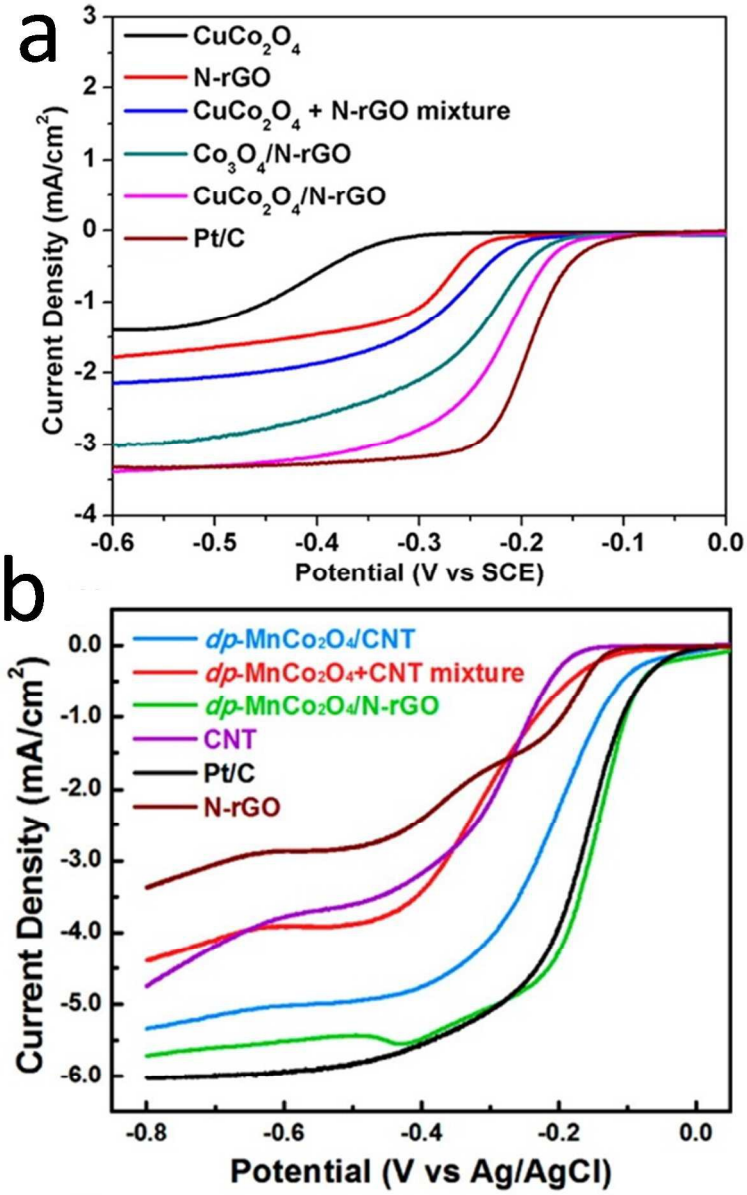

Figure 15. Linear sweep voltammetry (LSV) curves of different catalysts during ORR. (a) $CuCo_2O_4$/N-rGO hybrid, $CuCo_2O_4$ + N-rGO mixture, Co_3O_4/N-rGO hybrid, $CuCo_2O_4$, N-rGO, and Pt/C in an O_2-saturated 1 M KOH solution at 1600 rpm. (b) dp-$MnCo_2O_4$, dp-$MnCo_2O_4$/CNT hybrid, dp-$MnCo_2O_4$/N-rGO hybrid, mechanically mixeddp-$MnCo_2O_4$ + CNT, CNT, N-rGO, and Pt/C in a 0.1 M KOH aqueous solution, with the rotating rate of 2000 rpm.

Figures (a and b) have been reproduced from the ref 155 and ref.147 respectively with permission of American Chemical Society.

Sun and coworkers reported the synthesis of spinel $CuCo_2O_4$/N-rGO hybrid and observed that compared to simple physical mixture of $CuCo_2O_4$ and N-rGO or Co_3O_4/N-rGO exhibits better ORR activity with good durability[155]. ORR onset potential of $CuCo_2O_4$/N-rGO hybrid (−0.14 V) was 30mV more positive than Co_3O_4/N-rGO hybrid, as the copper substitution increases the number of actives sites in the hybrid (Figure 15a). $CuCo_2O_4$ alone shows poor ORR, the improved performance of hybrid is attributed to strong covalent interactions between N-rGO and $CuCo_2O_4$. Synergic covalent coupling between dp-$MnCo_2O_4$ and N-rGO enhances ORR activity of the dp-$MnCo_2O_4$ (Figure 15b) and leads to a promising candidate for Pt replacement for ORR[147].

Zhang et al prepared $NiCo_2O_4$-rGO hybrid by growing Ni-Co-glycolate on the surface of graphene oxide sheets followed by heat treatment with preferred nucleation sites arising from the coordination effect. In alkaline conditions, the hybrid is much more ORR active than individual $NiCo_2O_4$ or rGO components. The rotating disk electrode (RDE) measurements of the hybrid shows ORR current density −1.08 mA cm^{-2} at −0.349 V vs. Ag/AgCl and reaches about −2.0 mA cm^{-2} at the potential of −0.8 V at 2500 rpm which is highly phenomenal value. From the Koutecky–Levich (K–L) plots, the n value (number of electrons involved per O_2 in ORR) is 3.8 suggesting a four electron process for $NiCo_2O_4$ -rGO hybrid whereas for rGO and $NiCo_2O_4$ the n values are 1.8 and 2.6 respectively. The excellent ORR activity is attributed to the very strong coupling between the $NiCo_2O_4$ nanoparticles and rGO sheets[156]. Monodisperse 10nm M (II) substituted magnetite $MxFe_{3-x}O_4$ (M = Mn, Fe, Co, Cu) NPs were synthesized and their carbon (C) supported C- $M_xFe_{3-x}O_4$ samples were studied for ORR activity in alkaline media[157]. Among these, $Mn_xFe_{3-x}O_4$ was found to be highly active for ORR followed by $Co_xFe_{3-x}O_4$, $Cu_xFe_{3-x}O_4$, and Fe_3O_4. In CV, a large positive shift of onset reduction potential from C-Fe_3O_4 (−0.210 V) to C-$MnFe_2O_4$ (−0.322 V) was observed. $MnFe_2O_4$ has high ORR with the half-wave potential at −0.154 V, close to that from the commercial Pt (−0.137 V). The compositional study in $Mn_xFe_{3-x}O_4$ revealed that when X = 1 (that is $MnFe_2O_4$) the highest ORR (half-wave potential at −0.154 V) was achieved. Mn−ferrite NPs show a pair of redox peaks in the range of −0.077 to 0.062 V due to Mn(III)/Mn(II). Compared to other M(II) in M(II)− ferrite NPs described, Mn(II)

has higher tendency to adsorb O_2 and to transfer electrons to O_2 to regenerate Mn(III) which is responsible for the excellent ORR performance of C-$MnFe_2O_4$. Cost effective, noble metal free graphene (G) supported Co/CoO/$CoFe_2O_4$/G catalyst was developed as an alternative for Pt for ORR activity. Layered double hydroxides of cobalt, iron with graphene (CoFe-LDH-G) were used as precursors and their thermal treatment leads to Co/CoO/$CoFe_2O_4$/G catalyst. The catalyst exhibits a distinct ORR peak at -0.163 V is observed in O_2 saturated solution. The half wave potential of -0.25V vs. Ag/AgCl, only 50 mV negative than Pt/C was observed for Co/CoO/$CoFe_2O_4$/G catalyst. It is the cobalt atoms that act as active catalytic sites and with graphene support pronounced ORR activity was obtained[158].

La-Mn based perovskites with carbon (C-$LaMnO_3$) were prepared by reverse micellar (RM) route and compared their ORR activity with the carbon supported sample prepared through mechanical mixing. As the number of reactive sites in sample prepared through RM are larger and possess high surface area, it exhibits high ORR performance. When Ca and Fe were substituted in A and B sites of perovskite as $La_{0.4}Ca_{0.6}Mn_{0.6}Fe_{0.4}O_3$ with carbon support it exhibits superior ORR activity than carbon-supported $LaMnO_3$ and $LaMn_{0.6}Fe_{0.4}O_3$ with much durability under strong alkaline conditions. Especially Ca substitution at A site increases the number of valence states in B leading to enhanced ORR[159].

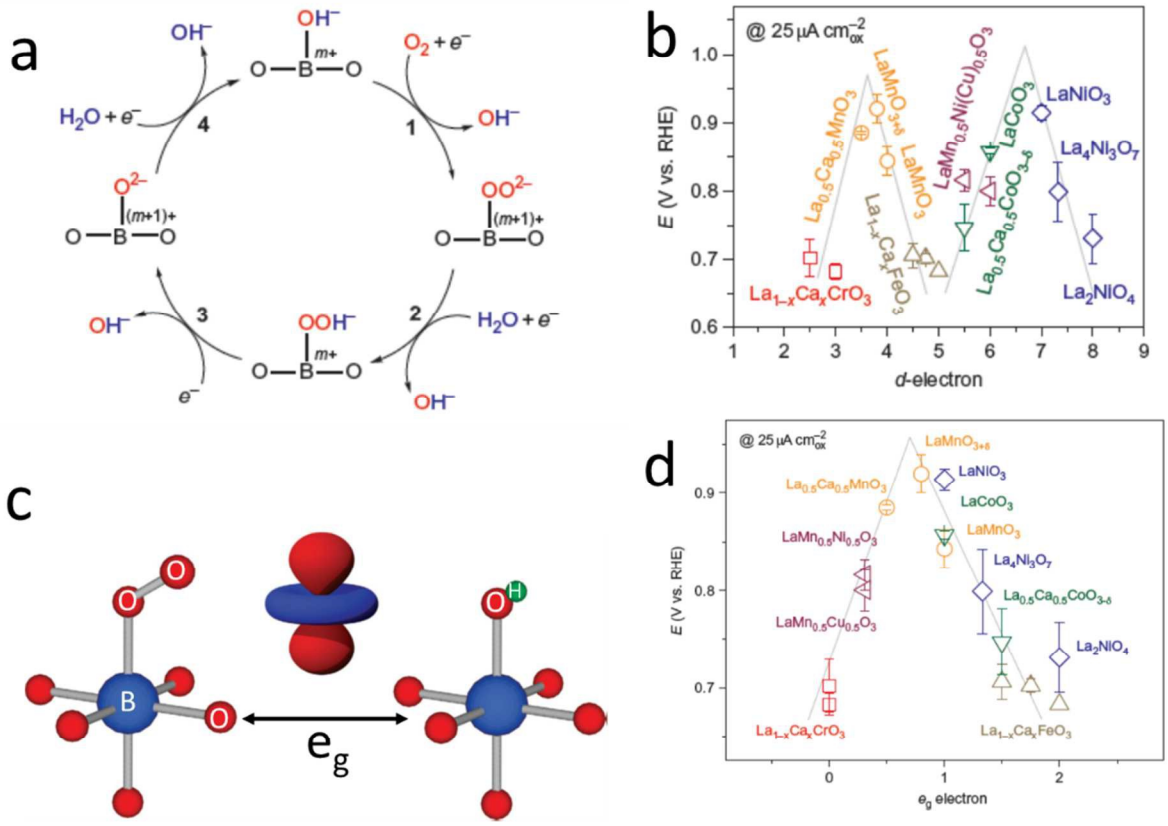

Figure 16. ORR activity of perovskite metal oxides. (a) Proposed ORR mechanism on perovskite oxide catalysts via four steps: 1, surface hydroxide displacement; 2, surface peroxide formation; 3, surface oxide formation; 4, surface hydroxide regeneration. (b) Potentials at 25 mA cm-2 ox of the perovskite oxides have an M-shaped relationship with d-electron number. Data symbols vary with type of B ions (Cr, red; Mn, orange; Fe,grey; Co, green; Ni, blue; mixed compounds, purple), where x=0 and 0.5 for Cr, and 0, 0.25 and 0.5 for Fe. (c) The shape of the e_g electron points directly towards the surface O atom and plays an important role during O_2^{2-}/OH^- exchange. (d) Potentials at 25 mA cm^{-2} ox as a function of e_g orbital in perovskite-based oxides. Data symbols vary with type of B ions (Cr, red; Mn, orange; Fe, grey;Co, green; Ni, blue; mixed compounds, purple), where x=0 and 0.5 for Cr, and 0, 0.25 and 0.5 for Fe. Reproduced from the ref. 160 with permission from Nature publishing group.

Suntivich et al. demonstrated ORR activity of perovskite-based oxides with various A-site ($La_{1-x}Ca_xBO_3$, $La_{1+x}BO_{3+x}$) and B-site ($LaB_{1-x}B'_xO_3$) substitutions with a correlation between σ*-orbital (e_g) occupation and the extent of B-site metal–oxygen covalency[160]. Proposed mechanism for the ORR activity of these perovskites follows 4 e^- transfer and the O_2^{2-}/OH^- exchange takes place at the B sites (Figure 16a). The ORR activity depends on the d- electron number per B cation and follows M-shape with d-electrons (Figure 16b). These perovskites with transition metal at B sites are very good for ORR activity due to greater hybridization between the e_g

orbital of bulk transition-metal ions (B site) and a molecular orbital of surface oxygen. In perovskites, e_g filling have a value of ~1 and increasing covalency between the metal 3d and oxygen 2p orbitals are important factor for excellent ORR activity (Figure 16c, d).

Han et al prepared a series of calcium-manganese-oxides, perovskite type $CaMnO_3$, layered structure $Ca_2Mn_3O_8$, post-spinel $CaMn_2O_4$ and $CaMn_3O_6$ with porous microsphere morphology[161].

Table 1. Electrochemical results during ORR for the Ca–Mn–O series and the benchmark Pt/C. Reproduced from the ref. 161 with permission of the Royal Society of Chemistry.

Catalyst	E_{onset} (V)	E_{half} (V)	I_s (mA cm^{-2})	I_m (mA mg^{-1})	n
$CaMnO_3$	0.96	0.76	−5.79	62.7	3.96
$Ca_2Mn_3O_8$	0.85	0.70	−3.54	38.3	3.53
$CaMn_2O_4$	0.85	0.69	−3.71	40.2	3.50
$CaMn_3O_6$	0.95	0.78	−4.43	48.0	3.86
Pt/C	0.99	0.84	−6.17	66.8	3.98

E_{onset}, E_{half}, I_s, I_m, and n denote onset potential, half-wave potential, specific current, mass current density and electron transfer number, respectively. I_s, I_m, and n correspond to values determined at 0.5 V.

As can be seen from the table $CaMnO_3$ and $CaMn_3O_6$ both are highly active, except low reduction current they exhibit properties similar to Pt/C. $Ca_2Mn_3O_8$ and $CaMn_2O_4$ exhibit poor electrochemical performance. Surface oxidation state of Mn and crystallographic structure are the two parameters that affect O_2 activation and in turn ORR activity. $CaMnO_3$ and $CaMn_3O_6$ have average surface Mn valence between +3 and +4 and $CaMnO_3$ with corner sharing MnO_6 octahedra provides (1×1) tunnels with comparable size to O-O bond length (0.12nm) of molecular oxygen to benefit ORR. While $CaMn_2O_4$ with low reducibility and sheet like denser MnO_6 octahedra is unfavorable for oxygen adsorption makes it less efficient ORR catalyst[161].

Summary and outlook

The continuous exploration of new phases as potentially improved catalysts has been entirely application-driven with the urge to develop clean source of energy either photo or electro-catalytically. This perspective underline the basic research conducted on metal oxides and their various hybrids both in terms of structure and compositions. The need to establish the link between the fundamentals of the mechanism to a commercial working model in order to maximize the efficiency still remains unresolved. We have outlined the key points of our discussion on heterogeneous catalysis separately for photo & electro catalysis.

In general, photocatalytic process comprises of a sequence of multiple steps which could either be synergistic or a competing step and it is equally challenging to identify which factor (s) dominates the overall activity. The multiple steps includes light harvesting, charge generation, separation, transportation, recombination and utilization .The efficacies of catalysts towards photocatalytic dye degradation was reviewed and new strategies were developed to improve the activity of photocatalytic systems especially for the visible-light-responsive photocatalysts, and active sites (co-catalysts) on photocatalysts which are observed to enhance the activity by many folds. Several methodologies have been developed to design the catalyst in order to improve light absorption, charge separation and transfer processes along with the integration with co-catalysts. However, the development of a photocatalyst with a wider absorption band is still needed. This perspective will provide an understanding of how the semiconductor nano-architectures can integrate multiple functional components for a highly efficient and stable photocatalyst.

We have presented several metal oxides and their hybrids as electrocatalysts for HER, OER and ORR reactions. The mechanism and thermodynamics of HER reveal that the best catalyst should be the one that binds in such a way that there is no sink or barrier in going from reactant to product through intermediate. Doping of high valent metal ions in oxides leads to defects or oxygen vacancies that will enhance the current density of the catalysts. In perovskites (ABO3), synergistic interactions between A site metal ion and B site metal ion were found to improve the catalytic activity. Size and shape plays vital role in deciding the activity. , and we have also discussed the shape dependent electrocatalytic activity. Among these shapes, the one with certain exposed facets/planes was found to exhibit high activity. The metal oxide or hybrid with definite chemical composition, its electronic structure and their surface atomic arrangement influence the

electrochemical performance. Large surface area, high porosity and high active site density were found to improve the activity. Spinels have metals with variable valence states and their structural flexibility also helps in fine tuning the electro catalytic activity. Perovskites with transition metal at B site, e_g filling having a value of nearly unity and increasing covalency between metal 3d and oxygen 2p orbitals are observed as important factors for excellent ORR performance. Orientation (end on/ parallel) of O2 molecules absorbed on catalyst surface also plays important role leading to higher ring current in ORR. Metal oxides combined with nanocarbon species such as graphene, carbon nanotubes (CNTs) improves the electrocatalytic activity, durability and high electrochemical stability due to their excellent conductivity and large surface area. The strong covalent interactions between nanocarbon support and metal oxides was found to be the reason for enhanced activity.

There is a need to develop a generalized method which is simple and green in nature for the synthesis of metal oxides and their hybrids with good control over composition, phase, size, shape and with desirable exposed facets. The inherent structure related details associated with electrocatalytic activity need to be addressed more thoroughly. There are several proposed mechanisms involving HER, OER and ORR, one simplified, convenient mechanism needed in each property such that catalysts can be developed on this basis. Non precious metals, oxides and their hybrids are studied under alkaline conditions. Electrochemical stability and durability are two concerns which needs to be addressed to improve the performance of electrocatalytic water splitting devices, fuel cells, metal air batteries, supercapacitors, chlor-alkali industries as they are associated with energy conversion and storage.

Acknowledgements

AKG thanks Department of Science & Technology, Govt. of India for financial support. KO thanks UGC, Govt. of India for the fellowship.

References:

(1). (a) M. R. Hoffmann, S. T. Martin, W. Choi, and D. W. Bahneman *Chem. Rev*. 1995, **95**, 69.

(2). Appl, M. 2006. Ammonia. *Ullmann's Encyclopedia of Industrial Chemistry*.

(3). H. Gleiter, *Nanostruct. Mater.* 1995, ***6,*** 3.

(4). E. Roduner *Chem. Soc. Rev*., 2006, **35**, 583

(5). M. Valden, X. Lai and D.W. Goodman, *Science* 1998, **281**, 1647.

(6). J.A. Rodriguez, G. Liu, T.H. Jirsak, Z. Chang, J. Dvorak and A. Maiti, *J. Am. Chem. Soc.* 2002, **124**, 5247.

(7). M. Baumer and H. J. Freund, *Progress. Surf. Sci.* 1999, **61**, 127.

(8). M.L Trudeau and J.Y. Ying, *Nanostruct. Mater.* 1996, **7**, 245.

(9). P. Moriarty, *Rep. Prog. Phys*. 2001, **64**, 297.

(10). J.A. Rodriguez, *Theor. Chem. Acc*. 2002, **107**, 117.

(11). J.A. Rodriguez, S. Chaturvedi, M. Kuhn and J. Hrbek, *J. Phys. Chem. B*. 1998, **102**, 5511.

(12). A. I. Hochbaum and P. Yang, *Chem. Rev*., 2010, **110**, 527.

(13). H. A. Atwater and A. Polman, *Nature Mater*., 2010, **9**, 205

(14). R. Marschall*, Adv. Funct. Mater.,* 2014, **24**, 2421

(15). A. Kubacka, M. Fernandez-García and G. Colon, *Chem. Rev*. 2012, **112**, 1555.

(16). K. Maedaa, *J. Photochem. Photobio. C: Photochem. Rev,* 2011, **12,** 237.

(17). T. Hisatomi, J. Kubota and K. Domen *Chem. Soc. Rev.,* 2014, **43**, 7520.

(18). M. Batzill, *Energy Environ. Sci.*, 2011, **4**, 3275.

(19). Y. Matsumoto, *J. Solid State Chem*., 1996, **126**, 227.

(20). B. Ohtani, *Phys.Chem.Chem.Phys*.2014, **16**, 1788.

(21). J. A. Rodriguez and M. Ferna´ndez-Garcı´a, *Synthesis, properties, and applications of oxide nanomaterials*, Wiley-Interscience, 2007.

(22). Q. Zhang, E. Uchaker, L. Stephanie, Candelaria and G. Cao, *Chem. Soc. Rev*., 2013, **42**, 3127.

(23). M. Fernandez-Garcı, A. Martınez-Arias, J. C. Hanson, and J. A. Rodriguez *Chem. Rev.* 2004, **104**, 4063.

(24). A. Fujishima and K. Honda, *Nature*, 1972, **23**, 837.

(25). M. Miyauchi, A. Nakajima, T. Watanabe and K. Hashimoto, *Chem. Mater*., 2002, **14**, 2812.

(26). F. E. Osterloh *Chem. Mater.*, 2008, **20**, 35.

(27). A. Y. Ahmed, T. A. Kandiel, T. Oekermann, and D. Bahnemann, *J. Phys. Chem. Lett*. 2011, **2**, 2461.

(28). H. Zhou, Y. Qu, T. Zeida and X. Duan *Energy Environ. Sci*., 2012, **5**, 6732.

(29). M. Ni, M. K. H. Leung, D. Y. C. Leung and K. Sumathy, *Renewable Sustainable Energy Rev*., 2007, **11**, 401.

(30). J. Choi, H. Park and M. R. Hoffmann, *J. Phys. Chem. C*, 2010, **114**, 783.

(31). Z. Kang, Y. Liu, C. H. A. Tsang, D. D. D. Ma, X. Fan, N.-B. Wong and S.T. Lee, *Adv. Mater*., 2009, **21**, 661.

(32). T. Ohmori, H. Mametsuka and E. Suzuki, *Int. J. Hydrogen Energy*, 2000, **25**, 953.

(33). R. Costi, G. Cohen, A. Salant, E. Rabani and U. Banin, *Nano Lett*.,2009, **9**, 2031.

(34). K. Maeda, K. Teramura, D. Lu, T. Takata, N. Saito, Y. Inoue and K. Domen, *Nature*, 2006, **440**, 295.

(35). K. Maeda, T. Takata, M. Hara, N. Saito, Y. Inoue, H. Kobayashi and K. Domen, *J. Am. Chem. Soc.*, 2005, **127**, 8286.

(36). K. Hashimoto, H. Irie and A. Fujishima, *Jpn. J. Appl. Phys*., 2005, **44**, 8269.

(37). O. Carp, C. L. Huisman and A. Reller, *Prog. Solid State Chem*., 2004, **32,** 33.

(38). M. A. Fox and M. T. Dulay, *Chem. Rev*., 1993, **93**, 341.

(39). L. Gomathi Devi and R. Kavitha, *Appl. Catal., B: Environmental*, 2013, **559**,140.

(40). T. Sreethawong, S. Laehsalee and S. Chavadej, *Int. J. Hydrogen Energy*, 2008, 33, 5947.

(41). Q. Xiang, J. Yu, W. Wang and M. Jaroniec, *Chem. Commun*., 2011, **47**, 6906.

(42). (a) G.R. Bamwenda, S. Tsubota, T. Nakamura and M. Haruta, *J. Photochem. Photobiol. A* 1995, **89**, 177. (b) T. Chen, Z. Feng, G. Wu, J. Shi, G. Ma, P. Ying, and C. Li, *J. Phys. Chem. C*, 2007, 111, 8005.

(43). A. Patsoura, D. I. Kondarides and X. E. Verykios, *Catal. Today*, 2007, **124**, 94.

(44). A. Naldoni, M. D. Arienzo, M. Altomare, M. Marelli, R. Scotti, F. Morazzoni, E. Sellia, and V. D. Santo, *Appl. Catal. B: Environmental*, 2013, **239,** 130.

(45). Z. Zhang, F. Xiao, Y. Guo, S. Wang and Y. Liu, *ACS Appl. Mater. Interfaces*, 2013, **5**, 2227.

(46). P. Wang, J. Wang, T. Ming, X. Wang, H. Yu, J. Yu, Y. Wang and M. Lei, *ACS Appl. Mater. Interfaces*, 2013, **5**, 2924.

(47). S. R. Morrison and T. Freund, *J. Chem. Phys*., 1967, **47**, 1543.

(48). S. R. Lingampalli, U. K. Gautam and C. N. R. Rao *Energy Environ. Sci*., 2013, **6**, 3589.

(49). X. Lu, G. Wang, S. Xie, J. Shi, W. Li, Y. Tong and Yat Li *Chem. Commun*., 2012, **48**, 7717.

(50). G. M. Wang, X. Y. Yang, F. Qian, J. Z. Zhang and Y. Li, *Nano Lett*., 2010, **10**, 1088.

(51). I. Gonzalez-Valls and M. Lira-Cantu, *Energy Environ. Sci.,* 2009, **2**, 19.

(52). K. G. Kanade, B. B. Kale, J. O. Baeg, S. M. Lee, C. W. Lee, S. J. Moon and H. J. Chang, *Mater. Chem. Phys.,* 2007, **102**, 98.

(53). R. M. Navarro, F. del Valle and J. L. G. Fierro, *Int. J. Hydrogen Energy*, 2008, **33**, 4265.

(54). X. Wang, G. Liu, Z. G. Chen, F. Li, L. Z. Wang, G. Q. Lu and H-M. Cheng, *Chem. Commun.*, 2009, 3452.

(55). X. Wang, L. C. Yin, G. Liu, L. Z. Wang, R. Saito, G. Q. Lu and H-M. Cheng, *Energy Environ. Sci.*, 2011, **4**, 3976.

(56). H. J. Snaith and L. Schmidt-Mende, *Adv. Mater.*, 2007, **19**, 3187.

(57). F.-X. Xiao, *ACS Appl. Mater. Interfaces,* 2012, **4**, 7055.

(58). W. Liu, M. Wanga, C. Xu, S.Chen and X. Fu, *J. Mol. Catal. A: Chemical,* 2013, **9**, 368.

(59). S. Balachandran and M. Swaminathan, *Dalton Trans.,* 2013, **42**, 5338.

(60). Q. P. Luo, X. Y. Yu, B. X. Lei, H. Y. Chen, D. B. Kuang, and C.-Y. Su, *J. Phys. Chem., C,* 2012, 116, 8111.

(61). R. C. Pawar and C. S. Lee, *Appl. Catal., B: Environmental,* 2014,**144**, 57.

(62). T-D. Nguyen, C-T. Dinh and T-O. Do, *Nanoscale*, 2011, **3**, 1861.

(63). M. R. Hoffmann, et al., *Chem. Rev*., 1995, **95**, 69.

(64). M. Machida, J. Yabunaka and T. Kijima, *Chem. Mater*., 2000, **12**, 812.

(65). H. Kato and A. Kudo, *Catal. Today*, 2003, **78**, 561.

(66). D. W. Hwang, H. G. Kim, J. Kim, K. Y. Cha, Y. G. Kim and J. S. Lee, *J. Catal.*, 2000, **193**, 40.

(67). 12 T. Ishihara, H. Nishiguchi, K. Fukamachi and Y. Takita, *J. Phys. Chem. B*, 1999, **103**, 1.

(68). Y. Hosogi, Y. Shimodaria, H. Kato, H. Kabayashi and A. Kudo, *Chem. Mater*., 2008, **20**, 1299.

(69). T. Xu, X. Zhao and Y. Zhu, *J. Phys. Chem. B*, 2006, **110**, 25825.

(70). H. Kato and A. Kudo, *Chem. Phys. Lett.*, 1998, **295**, 487.

(71). D. Das and A. K. Ganguli, *RSc. Adv*. 2013, **3**, 21697.

(72). T. Ikeda, S. Fujiyoshi, H. Kato, A. Kudo and H. Onishi*, J. Phys. Chem. B*, 2006, **110**, 7883.

(73). A. Kudo, H. Kato and S. Nakagawa, *J. Phys. Chem. B*, 2000, **104**, 571.

(74). R. Abe, M. Higashi, K. Sayama, Y. Abe and H. Sugihara, *J. Phys. Chem. B*, 2006, **110**, 2219.

(75). R. Abe, M. Higashi, Z. Zou, K. Sayama, Y. Abe and H. Arakawa, *J. Phys. Chem. B*, 2004, **108**, 811.

(76). A. J. Maria, K. L. Yeung, C. Y. Lee, P. L. Yue and C. K. Chan, *J. Catal.,* 2000, **192**, 185.

(77). C. Zhang and Y. Zhu, *Chem. Mater.*, 2005, **17**, 3537.

(78). L. G. Devi, B. N. Murthy and S. G. Kumar, *Chemosphere*, 2009, **76**, 1163.

(79). M. Sharma, D. Das, A. Baruah, A. Jain, and A. K. Ganguli, *Langmuir*, 2014, **30**, 3199.

(80). Y. Bi, S. Ouyang, J. Cao and J. Ye, *Phys. Chem. Chem. Phys.,* 2011, **13**, 10071.

(81). X. Wang, K. Maeda, A. Thomas, K. Takanabe, G. Xin, J. M. Carlsson, K. Domen and M. Antonietti, *Naure Mater.,* 2009, **8**, 76.

(82). R. Asahi, T. Morikiwa, T. Ohwaki, K. Aoki and Y. Taga, *Science*, 2001, **293**, 269.

(83). A. Thomas, A. Fischer, F. Goettmann, M. Antonietti, J. O. Muller, R. Schlogl and J. M. Carlsson, *J. Mater. Chem.*, 2008, **18**, 4893.

(84). J. Hu, W. Cheng, S. Huang, D. Wu and Z. Xie, *Appl. Phys. Lett.*, 2006, **89**, 261117.

(85). S. Meng, X. Ning, T. Zhang, S-F. Chen and X. Fu, *Phys. Chem. Chem. Phys.,* 2015, **17**, 11577.

(86). S. Kumar, A. Baruah, S. Tonda, B. Kumar, V. Shanker and B. Sreedhar, *Nanoscale*, 2014, **6**, 4830.

(87). S. Kumar, T. Surendar, A. Baruah and V. Shanker *J. Mater. Chem. A*, 2013, **1**, 5333.

(88). (a) K. Li, B. Chai, T. Peng, J. Mao, and L. Zan, *ACS Catal.* 2013, **3**, 170. (b) W. Zhou, H. Liu, J. Wang, D. Liu, G. Du, and J. Cui, *ACS Appl. Mater.Interfaces.*2010, **2**, 2385.

(89). J. Tian , Y. Sang , Z. Zhao , W. Zhou , D. Wang , X. Kang , H. Liu , J. Wang , S. Chen, H. Cai and H. Huang. *Small*, 2013, **9***,* 3864.

(90). G. R. Bamwenda , T. Uesigi , Y. Abe , K. Sayama , H. Arakawa , *Appl. Catal. A* 2001, **205**, 117.

(91). Z. Zhang, F. Xiao, Y. Guo, S. Wang and Y. Liu, *ACS Appl. Mater. Interfaces*, 2013, **5**, 2227.

(92). P. Wang, J. Wang, T. Ming, X. Wang, H. Yu, J. Yu, Y. Wang and M. Lei, *ACS Appl. Mater. Interfaces* 2013, **5**, 2924.

(93). R. Chalasani and S. Vasudevan, *ACS Nano,* 2013, **7**, 4093.

(94). Y. Wang, Q. Wang, X. Zhan, F. Wang, M. Safdar and J. He, *Nanoscale*, 2013, **5**, 8326.

(95). H. Gerischer and M.Luebke, *J. Electroanal. Chem.* 1986, **204**, 225.

(96). I. Robel, V. Subramanian, M. Kuno and P. V. Kamat, *J. Am. Chem. Soc.* 2006, **128**, 2385.

(97). R. Plass, P. Serge, J. Krüger and M. Grätzel, *J. Phys. Chem. B,* 2002, **106**, 7578.

(98). J. L. Blackburn, D. C. Selmarten, R. J. Ellingson, M. Jones, O. Micic and A. J. Nozik, *J. Phys. Chem. B* 2005, **109**, 2625.

(99). Y. Xie, S. H. Heo, Y. N. Kim, S. H. Yoo and S. O. Cho, *Nanotechnology* 2010, **21**, 015703.

(100). R. Vogel, P. Hoyer and H. Weller, *J. Phys. Chem.* 1994, **98**, 3183.

(101). S. Khanchandani, S. Kundu, A. Patra and A. K. Ganguli, *J. Phys. Chem. C*, 2012, **116**, 23653.

(102). S. Kumar, S. Khanchandani, M. Thirumal, and A. K. Ganguli, *ACS Appl. Mater. Interfaces*, 2014, **6**, 13221.

(103). S. Khanchandani, S. Kundu, A. Patra and A. K. Ganguli, *J. Phys. Chem. C* 2013, **117**, 5558.

(104). Y. Bu, Z. Chen, W. Li, and J. Yu, *ACS Appl. Mater. Interfaces*, 2013, **5**, 5097.

(105). J. Jean, S. Chang, P. R. Brown, J. J. Cheng , P. H. Rekemeyer, M. G. Bawendi, S. Gradecˇak, and V. Bulovic, *Adv. Mater.* 2013, **25**, 2790.

(106). S. Balachandran and M. Swaminathan, *Dalton Trans*. 2013, **42**, 5338.

(107). M. Basu, A. K. Sinha, M. Pradhan, S. Sarkar, Y. Negishi, Govind, and T. Pal, *Environ.Sci. Technol.* 2010, **44**, 6313.

(108). Y. Zhang, J. Tian, H. Li, L. Wang, X. Qin, A. M. Asiri, A. O. Al-Youbi and X. Sun, *Langmuir*, 2012, **28**, 12893.

(109). M. Basu, N. Garg and A. K. Ganguli, *J. Mater. Chem. A*, 2014, **2**, 7517.

(110). A. Kim, Y. Won, K. Woo, C-H. Kim, and J. Moon, *ACS Nano,* 2013, **7**, 1081.

(111). C. Gu, C. Cheng, H. Huang, T. Wong, N. Wang, and T-Y. Zhang, *Cryst. Growth Des.*2009, **9**, 3278.

(112). P. Roy, A. P. Periasamy, C-T. Liang and H-T. Chang, *Environ. Sci. Technol.* 2013, **47**, 6688.

(113). J. A. Rodriguez and M. Ferna´ndez-Garcı´a, *Synthesis, properties, and applications of oxide nanomaterials*, Wiley-Interscience, 2007.

(114). Q. Zhang, E. Uchaker, S. L. Candelariaz and G. Cao, *Chem. Soc. Rev.,* 2013, **42**, 3127.

(115). M. Ferna´ndez-Garcı, A. Martı´nez-Arias, J. C. Hanson and J. A. Rodriguez, *Chem. Rev.* 2004, **104,** 4063.

(116). D. Pletcher, "*A First Course in Electrode Processes*", The Electrochemical Consultancy, England, 1991.

(117). J. Lipkowski and P.N. Ross, *Electrocatalysis,* Wiley-VCH, Inc., 1998.

(118). S. H. Jordanov, P. Paunovic, O. Popovski, A. Dimitrov and S. Dragan, *Bull. Chem. Technol. Macedonia,* 2004, **23,** 101.

(119). J. O. M. Bockris, *J. Serbian Chem. Soc.,* 2005, **70**, 475.

(120). N. F. Atta, A. Galal and S. M. Ali, *Int. J. Electrochem. Sci.,* 2012, **7**, 725.

(121). T. R. Cook, D. K. Dogutan, S. Y. Reece, Y. Surendranath, T. S. Teets and D. G. Nocera, *Chem. Rev.*, 2010, **110**, 6474.

(122). Y. Liang, Y. Li, H. Wang and H. Dai, *J. Am. Chem. Soc.* 2013, **135**, 2013.

(123). Marc T. M. Koper, *J. Electroanalytical Chem.,* 2011, **660**, 254.

(124). J.K. Nørskov, J. Rossmeisl, A. Logadottir, L. Lundqvist, J.R. Kitchin, T. Bligaard, H. Jónsson, *J. Phys. Chem. B.*, 2004, **108**, 17886.

(125). X. Xie, W. Mu, X. Li, H. Wei, Y. Jian, Q. Yu, R. Zhang, K. Lv, H. Tang and S. Luo, *Electrochim. Acta,* 2014, **134**, 201.

(126). C. S. Lim, C. K. Chua, Z. Sofer, O. Jankovsky and M. Pumera, *Chem. Mater.,* 2014, **26**, 4130.

(127). Y. Yamada, K. Yano, Q. Xu and S. Fukuzumi, *J. Phys. Chem. C,* 2010, **114**, 16456.

(128). M. Gong, W. Zhou, M-C. Tsai, J. Zhou, M. Guan, M-C. Lin, B. Zhang, Y. Hu, D-Y. Wang, J. Yang, S. J. Pennycook, B-J. Hwang and H. Dai, *Nature Commun.*, 2014, **5**, 4695.

(129). K. Xiong, L. Li, Z. Deng, M. Xia, S. Chen, S. Tan, X. Peng, C. Duanb and Z. Wei, *RSC Adv.,* 2014, **4**, 20521.

(130). B. Kumar, S. Saha, M. Basu and A. K. Ganguli, *J. Mater. Chem. A,* 2013, **1**, 4728.

(131). B. Kumar, S. Saha, A. Ganguly and A. K. Ganguli, *RSC Adv.,* 2014, **4,** 12043.

(132). J. Suntivich, H. A. Gasteiger, N. Yabuuchi, H. Nakanishi, J. B. Goodenough and Y. Shao-Horn, *Nature chem.,* 2011, **3**, 546.

(133). A. J. Esswein, M. J. McMurdo, P. N. Ross, A. T. Bell and T. Don Tilley**,** *J. Phys. Chem. C,* 2009, **113**, 15068.

(134). N. Garga, Menaka, K. V. Ramanujachary, S. E. Lofland and A. K. Ganguli, *J. Solid State Chem.* 2013, **197**, 392.

(135). N. Garg, M. Basu, K. Upadhyaya, S. M. Shivaprasad and A. K. Ganguli, *RSC Adv.,* 2013, **3**, 24328.

(136). N. Garg, M. Basu, and A. K. Ganguli *J. Phys. Chem. C,* 2014, **118,** 17332.

(137). S. Sharma, N. Garg, K. V. Ramanujachary, S. E. Lofland, and A. K. Ganguli, *Cryst. Growth Des.,* 2012, **12**, 4202.

(138). J. Suntivich, K. J. May, H. A. Gasteiger, J. B. Goodenough and Y. Shao-Horn, *Science*, 2011, **334**, 1383.

(139). F. Cheng, J. Shen, B. Peng, Y. Pan, Z. Tao and J. Chen, *Nature Chem.,* 2011, **3**, 79.

(140). A. Ramírez, P. Hillebrand, D. Stellmach, M. M. May, P. Bogdanoff, and S. Fiechter, *J. Phys. Chem. C,* 2014, **118**, 14073.

(141). C. L. Charles, M. Crory, S. Jung, J. C. Peters and T. F. Jaramillo, *J. Am. Chem. Soc*., 2013, **135**, 16977.

(142). T. Maiyalagan, K. R. Chemelewski and A. Manthiram, *ACS Catal.*, 2014, **4**, 421.

(143). X. Liu, Z. Chang, L. Luo, T. Xu, X. Lei, J. Liu and X. Sun, *Chem. Mater.*, 2014, **26**, 1889.

(144). S. Chen and S-Z., Qiao, *ACS Nano.,* 2013, **7**, 10190.

(145). B. Cui, H. Lin, J.-B. Li, X. Li, J. Yang and J. Tao, *Adv. Funct. Mater,* 2008, **18,** 1440.

(146). X. Wu and K. Scott, *J. Mater. Chem.,* 2011, **21**, 12344.

(147). X. Ge, Y. Liu, F. W. Thomas Goh, T. S. Andy Hor, Y. Zong, P. Xiao, Z. Zhang, S. H. Lim, B. Li, X. Wang and Z. Liu, *ACS Appl. Mater. Interfaces,* 2014, **6,** 12684.

(148). S. Bag, K. Roy, C. S. Gopinath and C. Retna Raj, *ACS Appl. Mater. Interfaces,* 2014, **6**, 2692.

(149). X. Zhai, W. Yang, M. Li, G. Lv, J. Liu and X. Zhang, *Carbon,* 2013, **65,** 277.

(150). M. S. El-Deab and Takeo Ohsaka, *Angew. Chem. Int. Ed.,* 2006, **45,** 5963.

(151). S. Guo, S. Zhang, L. Wu and S. Sun, *Angew. Chem. Int. Ed.,* 2012, **51,** 11770.

(152). Q. Li, P. Xu, B. Zhang, H. Tsai, S. Zheng, G. Wu and H.-L. Wang, *J. Phys. Chem. C,* 2013, **117,** 13872.

(153). Z–S. Wu, S. Yang, Y. Sun, K. Parvez, X. Feng and K. Müllen, *J. Am. Chem. Soc.,* 2012, **134,** 9082.

(154). Y. Liang, H. Wang, J. Zhou, Y. Li, J. Wang, T. Regier and H. Dai, *J. Am. Chem. Soc*., 2012, **134**, 3517.

(155). R. Ning, J. Tian, A. M. Asiri, A. H. Qusti, O. Abdulrahman Al-Youbi and X. Sun, *Langmuir,* 2013, **29**, 13146.

(156). G. Zhang, B. Y. Xia, X. Wang and X. W. Lou, *Adv. Mater.*, 2014, **26**, 2408.

(157). H Zhu, S. Zhang, Y -X. Huang, L. Wu and S. Sun, *Nano Lett.*, 2013, 13, 2947.

(158). R. Huo, W-J. Jiang, S. Xu, F. Zhang and J-S. Hu, *Nanoscale,* 2014, **6,** 203.

(159). M. Yuasa, N. Yamazoe, and K. Shimanoe, *J. Electrochem. Soc.,* 2011, **158**, A411.

(160). J. Suntivich, H. A. Gasteiger, N. Yabuuchi, H. Nakanishi, J. B. Goodenough and Y. Shao-Horn, *Nature Chem.,* 2011, **3***,* 546.

(161). X. Han, T. Zhang, J. Du, F. Cheng and J. Chen, *Chem. Sci.,* 2013, **4**, 368.

Graphical Abstract

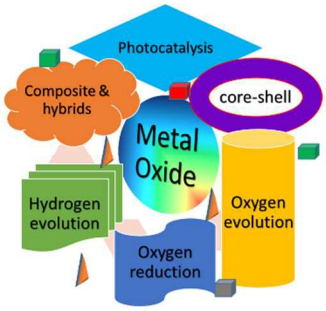

The enormous efforts on the design of efficient oxide based materials towards photo & electro catalysis has been emphasized in this article with emphasis on its size, structure & morphology.